# SEMI–AUTOMATED ANALYSIS OF FAULTS WITH METER–SCALE DISPLACEMENTS AND NETWORKS OF PLANAR FEATURES USING HIGH–RESOLUTION 3D SEISMIC TO INVESTIGATE GAS LEAKAGE AT THE VESTNESA RIDGE, EASTERN FRAM STRAIT

Frances Cooke[1]*, Andreia Plaza–Faverola[2], Stefan Bünz[2], Paul de Groot[3], David C. P. Peacock[4]

[1]Department of Geosciences, UiT the Arctic University of Norway, 9037 Tromsø, Norway, email: frances.a.cooke@uit.no
[2]iC3: Centre for ice, Cryosphere, Carbon and Climate, Department of Geosciences, UiT the Arctic University of Norway, 9037 Tromsø, Norway, emails: andreia.a.faverola@uit.no, stefan.buenz@uit.no
[3]dGB Earth Sciences BV, Enschede, The Netherlands, email: paul.degroot@dgbes.com
[4]Geoscience Centre of the University of Göttingen, Structural Geology & Geodynamics, Goldschmidtstraße 3, 37077 Göttingen, Germany, email: davidcppeacock@gmail.com

## ABSTRACT

We present a semi–automated method for extracting faults and other planar features from two high–resolution seismic volumes in the eastern Fram Strait. We assess seismic data quality and resolution prior to structural interpretation to determine the appropriate processing workflow. This workflow, designed for high–resolution data sets, identifies meter–scale (>3–4 m) faults and other planar features, picked up by subtle changes in the curvature and discontinuities of seismic reflections, to investigate their relationship with fluid migration in the shallow subsurface. Although evidence exists for Holocene (< ~8 Ka) fault–associated gas seepage, structures in both volumes are presently sealing. We assess structures based on those that have measurable throw (faults) and those that do not (planar features). Structures lacking measurable throw are significant because they appear to represent fluid flow pathways. This technique enhances the analysis of the geometries of the mapped structures, facilitating the interpretation of meter–scale fault throws and the orientations of planar features. We provide insights into the evolution of structures previously linked to episodes of fluid migration and gas leakage at the Vestnesa Ridge. We infer zones of dilation (i.e., opening) at locations where faults or networks of planar features interact and investigate how these structures influence localized uplift and shallowing of the interface between free–gas and gas hydrate (i.e., the bottom–simulating reflection).


## INTRODUCTION

Understanding fluid migration in the subsurface commonly requires knowledge about the structures (i.e., faults and networks of planar features) through which the fluids may migrate. Vital information can be provided by seismic data, which are prone to problems related to both

seismic resolution and interpreter bias. Methods that improve the interpretation of high–resolution (HR) seismic data can therefore help with the understanding of fluid flow in the near–surface (i.e., ~200 m below the seafloor (mbsf)). Here, an existing automated fault extraction method (see Appendix A, Table A–1 for definitions of terms) is applied to high–resolution P–Cable 3D (HR3D) seismic data to improve the interpretation of faults and planar features, and thereby improve the understanding of gas leakage. Manual interpretation alone would be worse at identifying faults and planar features because the data sets contain faults with offsets just above the seismic resolution and other structures that may be faults with throws just below the seismic resolution.

Methods involving manual interpretation of structures in 3D seismic data are challenging and time–consuming, and human bias is introduced through selective fault mapping (e.g., Bond et al., 2007; Bond 2015). Fault interpretation using 3D seismic data traditionally involves generation of fault surfaces by linking two–dimensional fault sticks picked on seismic sections and time– or depth–slices (e.g., Faleide et al., 2021). The resulting interpolated fault surface is often an inaccurate representation of the fault geometry and requires validation (Godefroy et al., 2018). To reduce uncertainty, empiric geologic rules are generally used in fault modeling for quality control. For example, Freeman et al. (2010) validate fault geometry by using a displacement model that assumes maximum displacement in the center of a fault and a linear decrease in displacement towards the fault tips (Godefroy et al., 2018). The interaction and linkage of fault segments means, however, that the maximum displacement point need not be at the center of a fault, and the displacement profile does not change smoothly to the tips (e.g., Peacock and Sanderson, 1991). The approach here, using an automated method, is not only useful for faults with throws below conventional seismic resolution (typically ~15 m) but also

other ambiguous features close to the seismic resolution, where measuring maximum displacement is not achieved. It is assumed that high "fault likelihood" (defined in Appendix A, Table A–1) represents the maximum displacement and the decrease towards the fault tips results in a disappearance in the fault, as displacement decreases below the resolution of the data set. Semi–automatic methods and automatic fault recognition methods are now common practice (e.g., Acuña–Uribe et al., 2021; Wang et al., 2022) to reduce the workload of manual interpretation and to avoid selective fault mapping.

The resolution and quality of the seismic data are key factors in fault mapping. Parts of faults, including fault tips and splays, are commonly below seismic detection levels (e.g., Faleide et al., 2021). The P–Cable seismic system (Planke et al., 2009), as used in this study, samples the data at high spatial (e.g., 6.25 m) and vertical (3–5 m) resolutions, focusing on a near offset range (50–150 m) to achieve the highest resolution. We have used machine learning (ML) to improve the structural analysis of the seismic data, involving automatic recognition of structures required for the interpretation.

The central theme of this work is the fluid migration system at the Vestnesa Ridge, an Arctic gas–charged deep marine sedimentary ridge, where gas leakage appears to be influenced by layer–bound deformed sediments (e.g., Cooke et al., 2023). Additional research is necessary, however, to understand how the deformed sedimentary units are interconnected. In this work, automatically extracted faults with meter–scale throws and planar features are assessed individually in terms of "fault plane" (defined in Appendix A, Table A–1) size and orientation (i.e., strike and dip). We also evaluate how these structures interact with nearby gas leakage features and how they may be influenced by the bathymetry and depth to the base of the gas hydrate stability zone, below which free gas is present. Even the absence of structures, such as

unresolved tips or seismic disturbances that obscure fault plane identification, provide useful information about the relationship between these structures and gas leakage.

This study provides a workflow for high–resolution structural interpretation in the near–surface and where gas hydrate and fluid migration result in disturbances to the seismic data. Vertical fluid migration structures are referred to here as "gas chimneys" (larger >100 m width) and "pipes" (smaller <100 m width). These are commonly related to present–day/paleo structural features linked to fluid release, including pockmarks (<60 – >600 m diameter), localized overpressure features (inferred from seismic data), and methane–derived authigenic carbonates (i.e., mounds; Himmler et al., 2019).

The main aim of the study is to illustrate how ML can be used to contribute to the standardization of semi–automatic meter–scale structural interpretation of the sub–seafloor, where manual methods are not suitable, thereby improving both the interpretation of structures and the understanding of controls on gas leakage.

## GEOLOGIC SETTING

### The Vestnesa Ridge

The Vestnesa Ridge is a 100 km long and 3–5 km wide contourite drift in the eastern Fram Strait at water depths between 1200–1700 m (Figure 1b). It comprises an eastern segment, characterized by a narrow crest, oriented NW–SE, and parallel to the Molloy Transform Fault (e.g., Eiken and Hinz 1993; Ritzmann et al., 2012). The central portion of the Ridge forms a plateau as it bends towards the west, striking ~ESE–WNW towards the Molloy Ridge. Towards the far west, it strikes NW–SE, parallel to the eastern segment. The Ridge lies between the ultra–

slow, obliquely spreading, Molloy and Knipovich Ridges (Figure 1b). Asymmetric discontinuous spreading segments oriented ~N–S to NE–SW at the northernmost extension of the Mid–Atlantic Ridge System are documented in magnetic data (i.e., the Knipovich Ridge; Dumais et al., 2020). Contourite deposits several km thick (>5 km in places) occur in the study area (Eiken and Hinz 1993; Crane et al., 2001; Vanneste et al., 2005; Osti et al., 2019), decreasing in thickness to hundreds of meters towards the Knipovich Transform Fault and the Molloy Transform Fault (Breivik et al., 1999; Ritzmann et al., 2004; Bünz et al., 2012).

*Chronostratigraphy*

The focus of this study is in the upper ~200 m of the sedimentary sequence, defined by the stratigraphic unit Yermak Plateau (YP)–3 (< ~2.7 Ma; Eiken and Hinz, 1993). It is characterized by alternating bioturbated fine–grained and ice–rafted debris–rich deposits, and laminated silty turbidites (e.g., Howe et al., 2008; Jessen et al., 2010; Consolaro et al., 2015; Sztybor and Rasmussen, 2017). This sequence thins from the central bend of the Ridge, where the YP–3 isopach is ~0.6 seconds TWT (Eiken and Hinz, 1993) (~600 m sedimentary package thickness) towards the western flank of the Ridge, where the YP–3 isopach is closer to ~0.4 seconds TWT (equivalent to ~400 m).

The 3D seismic data sets we use for this study were collected at the eastern and the western flanks of the YP–3 depocenter. They are located: (1) at the central bend of the Ridge, termed transition east–west i.e., “TEW–volume”; and (2) at the western segment of the Ridge i.e., “West–volume” (Figure 1).

*Fluid flow system*

A deep marine (>1000 m water depth) gas hydrate system (~140–200 m thick) is present along the entire Vestnesa Ridge (e.g., Bünz et al., 2012; Plaza–Faverola et al., 2017; Singhroha et al., 2019). This system is characterized by a well–defined bottom–simulating reflection (BSR) which delineates the boundary between gas hydrate bearing sediment and the underlying free gas trapped at the crest of the Vestnesa Ridge (Plaza–Faverola et al., 2017). Bottom water temperatures are approximately –0.5 °C and hydrostatic pressures at the BSR depth are around 14 MPa (Plaza–Faverola et al., 2017; Ramachandran et al., 2022). The presence of a <100 m thick free gas zone underneath the BSR has been documented based on low velocity and low resistivity anomalies (e.g., Hustoft et al., 2009; Petersen et al., 2010; Goswami et al., 2015; Singhroha et al., 2019). The BSR is characterized by anomalously high amplitudes and a phase reversal with respect to the seafloor polarity, indicating the presence of free gas trapped beneath gas hydrate–bearing strata (e.g., Figure 1f). The high amplitudes are commonly found at points where the BSR cross–cuts reflections at locations here termed "BSR–ridges" (also referred to in the literature as "BSR uplift" with associated high amplitude anomalies; e.g., Zhang et al., 2022). "BSR–high" is used here to describe the shallowest isochron depths between the seafloor and the BSR. HR3D seismic data reveal multi–stage buried (i.e., covered by younger sediments) pockmarks at both the eastern (excluded from this study) and western segments of the Vestnesa Ridge, indicating that recurrent seepage events have occurred recently (i.e., 8 Ka; Consolaro et al., 2015) and episodically along the entire Vestnesa Ridge (Plaza–Faverola et al., 2015; Knies et al., 2018; Himmler et al., 2019). Pockmarks are seafloor expressions of focused fluid flow, identified as gas chimneys and pipes in subsurface seismic data (Petersen et al., 2010; Bünz et al., 2012).

Evidence from seismic data for fracture–controlled seepage has been documented (Plaza–Faverola et al., 2015; Singhroha et al., 2020; Cooke et al., 2023). At present, seepage is restricted to the eastern segment of the Vestnesa Ridge (Figure 1f, Hustoft et al., 2009; Bünz et al., 2012) and is not recorded in the west (Plaza–Faverola et al., 2015). In the central bend (TEW–volume) of the Vestnesa Ridge, pockmarks are referred to as inactive or dormant (e.g., Cooke et al., 2023), although there is evidence for the presence of gas tens of meters below the seafloor (e.g., Sultan et al., 2020).

The relationship between gas chimneys/pipes and faults has been studied at the Vestnesa Ridge through the detection of gas hydrates in fractures (Singhroha et al., 2020), by documenting the variation in the morphology of gas chimneys through time and by describing their spatial relation to faults (Plaza–Faverola et al., 2015; Cooke et al., 2023).

Faults currently behave differently in the west of the Vestnesa Ridge compared to the eastern segment. Previous work emphasizes that advection (defined by fluid flow along faults that may act at greater depths, and at active chimneys) is the primary driver of fluid flow through the system at the eastern segment, while advection has probably been replaced with diffusive flow through the sediments at the bend of the ridge and towards the west, where the Ridge becomes more like a plateau (Plaza–Faverola et al., 2023). It is likely that the near–surface sediments are overpressured where fluid flow occurs by diffusion (Sultan et al., 2020). In this paper, we present maps of structures at the central ridge bend, and far west of the Vestnesa Ridge, where the structures are considered in this work as episodically sealed.

# DATA

Two high–resolution 3D (HR3D) P–Cable surveys are used in this study (Planke et al., 2009). These are the TEW– (~2 x 7 km) and West– (1.3 x 9 km) volumes (Bünz, 2022). The data were acquired and processed on board the R/V Helmer Hanssen in 2018 during the Centre for Arctic Gas Hydrate, Environment and Climate (CAGE) cruise 18–4 (Bünz, 2022). Seismic velocity models derived from ocean bottom seismometer (OBS) data (Petersen et al., 2010) were used to convert the seismic data into the depth domain. Further information on data acquisition and onboard pre–processing sequence is given by Bünz (2022) (also refer to Supplementary Tables S–1 and S–2). The vertical resolution is between ~3–4 m at the seafloor, calculated as $\lambda/4$ using a water velocity of 1,480 m/s and dominant frequencies of 120 Hz (TEW–volume) and 100 Hz (West–volume) (Supplementary Figure S–1). The lateral resolution of the 3D seismic volumes is defined by the spatial sampling (i.e., hydrophones separated by 3.125 m and a bin size of 6.25 x 6.25 m used for increasing trace fold). Every seismic trace represents energy averaged within the Fresnel Zone (FZ) (i.e., at the seafloor the FZ is ~85 m and ~100 m for the TEW– and West–volumes respectively). With a shooting rate of 4–5 seconds and a ship speed of 4–5 knots, however, we ensure that new energy is produced every 8–10 m. With a 3.125 m spacing between recorders, we can efficiently generate a source–receiver image point every ~1.5 m. Random noise levels are measured by subtracting a dip–steered median filter with a step out of 1 from the original data. This gives a signal to noise ratio (S/N) of 6 in the TEW–volume and 10 in the West–volume, indicating high quality seismic data in both volumes.

The data volumes are tied to available chronological markers derived from ODP wells (911A and 910C) on the Yermak Plateau, north of the Vestnesa Ridge (Hustoft et al., 2009;

Mattingsdal et al., 2014; Plaza–Faverola et al., 2017; Knies et al., 2018). A high–resolution 2D seismic line (Figure 1f) was used in this study to correlate chronostratigraphic markers for both seismic volumes, using results from previous work (Plaza–Faverola et al., 2015, 2017; Alexandropoulou et al., 2021; Dessandier et al., 2021; Cooke et al., 2023).

## METHODS AND WORKFLOWS

To interpret faults and other planar features, we utilized seismic data, employing advanced processing and analysis techniques to accurately delineate fault geometry and assess subsurface characteristics. A fault is typically defined by its displacement type (i.e., normal, reverse, strike–slip or oblique–slip; Anderson 1905), which relies on the fault having a measurable shear displacement. In this study, we refer to structures as being "faults" only where shear displacement is observed, and "planar feature" where no measurable shear displacement is observed (defined in Appendix A, Table A–1).

To enhance the accuracy and efficiency of fault identification, we implemented automated fault extraction techniques, to systematically detect and map structures within the seismic data set. Automated fault extractions have previously been achieved through discontinuity attributes such as edge–detection methods (e.g., Lisle 1994; Bahorich and Farmer, 1995; Marfurt et al., 1999; Roberts 2001), and through such algorithms as ant–tracking (Pedersen et al., 2002) or (the original) fault likelihood (Hale, 2013). Here we use ML fault likelihood, (e.g., de Groot et al., 2023) which is more suited to fluid flow interpretation than the original fault likelihood algorithm because the ML method does not display radial artefacts where

seismic traces are missing or where there are seismic disturbances such as chimneys (Supplementary Figure S–2).

Research using synthetic data sets to train ML models, as used here, is at an early stage (e.g., Wu et al., 2019). The ML method is the U–Net ("U–shaped" encoder–decoder "Network" architecture), first introduced in biomedicine by Ronneberger et al. (2015) and since incorporated into geophysical software. U–Net is a convolution type of Neural Network (CNN), used to improve automatic fault and fracture interpretation, as described by Wu et al. (2019). Here, we implement the 3D U–Net ML model, trained on simulated data, to predict the locations of synthetic faults and successfully tested on real 3D seismic data without the need for re–training (Wu et al., 2019; de Groot et al., 2023).

The automatically extracted structures are manually interpreted as faults if throw is observed, rendering the overall approach for data analysis semi–automatic. A selection of (~20) representative fault planes (selected according to whether they intersect seismic surfaces) are manually selected from each data set to systematically reduce numbers (entire volume number is ~200) and facilitate further analyses of fault plane evolution. The interpretation enables us to consider the implications for fluid flow of the fault and planar feature networks, including their interconnectivity (defined in Appendix A, Table A–1, and refer to Peacock et al., 2016). Many of the structures are, however, at the limits of the resolution, i.e., the structure is identified, but the displacement is probably below the resolution of the data sets. This means that the entire network has not been imaged. Scholz and Cowie (1990) demonstrate that patterns of fault displacement follow a consistent scaling relationship and indicate self–similar behavior across different scales of faulting (i.e., power–law scaling). This suggests that even though smaller faults may not be

fully resolved in the seismic data, the power–law scaling relationship means that these unresolved displacements contribute to the overall fault network and total strain.

*3D U–Net Machine Learning fault prediction*

The implementation of the ML 3D U–Net on our two HR3D seismic volumes allowed for more detailed analyses and interpretation of fault and planar feature networks. We use the term "fault detection" in this section because "fault" is a common broad term in geophysical software that is used for the detection of planar features (which can include artefacts). The output seismic data using the ML 3D U–Net in this study is referred to as the "Machine Learning Fault Likelihood" (MLFL) volume (defined in Appendix A, Table A–1). Detection of faults is an image segmentation task, where a 3D seismic image is labeled with ones on faults and zeros elsewhere (Di et al., 2018; Li et al., 2019; Wu et al., 2019; An et al., 2021). Here the model transforms a block of seismic data (128 x 128 x 128 samples) into a similar–size block of fault likelihood. In the application phase the output blocks are overlapping and blended in the overlap–zones. We discovered qualitatively that the ML version of the fault likelihood volume significantly improved the quality of the fault detection and reduced artefacts. Our observations confirm the findings of Wu et al (2019); not only is the ML 3D U–Net more computationally efficient than the original fault likelihood algorithm (Hale et al., 2013), which we initially tested and rejected (Supplementary Figure S–2), but it also tends to generate fewer artefacts. The U–Net model takes six minutes to predict faults in seismic volume with 320 x 1120 x 398 samples. Calculating the original fault likelihood is less computationally efficient (52 minutes) because it involves scanning through all possible combinations of fault strikes and dips to determine the maximum fault likelihoods, followed by the application of a thinning algorithm.

The performance of the ML 3D U–Net is highly dependent on the quality of the input data, and optimal data conditioning prior to fault extraction is important to reduce the enhancement of artefacts and to interpret clearer and more continuous faults (Chopra and Marfurt 2013; de Groot et al., 2021; Chen et al., 2022). Sail line artefacts were removed using fractional statics applied pre–stack (Bünz 2022) and residual statics post–stack (Cooke et al., 2023). We also applied an edge–preserving smoothing filter to the post–stack volume data sets (e.g., Luo et al., 2002; AlBinHassan et al., 2006) prior to running the 3D U–Net model to sharpen fault edges (Figure 2). Data conditioning after static correction (here using edge–preserving smoothing), however, commonly re–introduces sail line artefacts because of the sharpening of edges which is necessary prior to the application of the fault likelihood algorithm. HR3D data volumes that have significant static correction problems (frequently encountered when data are collected in rough seas) are more likely to have re–introduced sail line artefacts because of greater difficulties when initially removing them. The West–volume is affected more by re–introduced sail line artefacts than the TEW–volume, with artefacts particularly visible in the shallow horizons.

*Extraction of fault planes*

The fault extraction algorithm requires an input volume with three components: “fault likelihood”, “fault dip” and “fault strike” (defined in Appendix A, Table A–1, Figure 2 for the workflow). We must first compute the missing components: fault dip and fault strike because the 3D U–Net fault prediction model only predicts fault likelihood itself. Next, the fault extraction algorithm automatically creates a set of fault grids, referred to as “gridded surfaces” (Figure 2, Supplementary Figure S–3). The user controls the minimum size of the gridded surfaces and has

options to select and merge the surfaces for saving as fault planes. The gridded surfaces are merged to create smooth fault planes when dealing with relatively big faults in lower resolution data sets. In this study, merging is avoided because the variations in azimuth and dip are important from one related gridded surface to the next. A change in fault orientation is better represented by keeping the gridded surfaces separate, providing a more reliable result than averaging the fault plane values.

*Gas chimneys*

The chimneys were extracted using the seismic attribute "semblance" (i.e., seismic reflection continuity, e.g., Figure 3). The highly continuous background seismic data were rendered transparent to expose the chimneys selected in the study. Selected gas chimneys from the zones of interest were categorized based on whether they: 1) reach the present–day seafloor, 2) reached the seafloor in the past (i.e., paleo seafloor) or 3) have never reached the seafloor. In the latter case, it is not possible to determine when the gas chimney was active.

*Chronostratigraphic marker selection*

Chronostratigraphic markers dating from within the last ~1.5 million years (Ma) are used: H0.3 (~0.1 Ma), H1 (~0.2 Ma), H2 (~0.4 Ma), H2.25 (~1 Ma) and H3 (~1.5 Ma) (Cooke et al., 2023). The markers estimate respective (burial) ages of extracted fault planes (Figure 4). Some of the structures intersect multiple horizons and are categorized according to chronostratigraphic zones (oldest to youngest) defined by the age identities. The categories are Y–1 (Yellow), G–2 (Green), B–3 (Blue), O–4 (Orange), and P–5 (Pink), which intersect at least horizon H3, H2.25, H2, H1 and H0.3 respectively (Figure 4, Supplementary Tables S–3, and S–4). Note that some

fault planes are interpreted to intersect only one horizon while others intersect more than one. Only the features that intersect the horizons are considered and the throw on each fault plane is assessed. The fault planes that are situated between the chronostratigraphic horizons without intersecting them, and those that are located beneath the oldest horizon (i.e., those beneath the BSR in the West–volume) are excluded from the study. This reduces the number of fault planes from 198 (for each volume) at the semi–automatic fault plane extraction stage (Supplementary Figure S–3) to 23 for the TEW–volume and 26 for the West–volume, showing that many of the features were comparatively small and/or largely beneath the deepest horizon (H3).

*Fault selection*

After automatically extracting the fault planes and assigning an age identity, they were manually checked and categorized into those that have measurable throws and those that do not, to verify the ML 3D U–Net method (Supplementary Tables S–5 and S–6). Fault plane dip (° from the horizontal) and azimuth (° clockwise from north) are also documented (Supplementary Tables S–7 and S–8). The process involves creating composite lines from the HR3D volume that each cross–cut the structures to enable the manual estimation of meter–scale throw. Automating fault offsets was not possible because the throw values are so small (<3–15 m). Those features with fault likelihood values closest to 1 (i.e., the highest likelihood) are likely to have an offset visible in the vertical seismic (e.g., fault plane *8b* in the West–volume–(e), and fault plane *10* in the center of the TEW–volume, Figure 5). The fault plane is described as a "planar feature" where the throw is difficult to measure (e.g., fault plane *5* in the West–volume–(e), and fault plane *9a* in the TEW–volume–(e), Figure 5). In the latter two examples, seismic reflections crossing the planar feature are mostly bending and it is the curvature of the reflection that

verifies the fault plane. These structures are interpreted to have throws at or slightly below the limit of the seismic resolution. Manual interpretation of faults from seismic data typically relies on the interpreter identifying throws. In this work, we apply the MLFL method to extract all possible fault planes, including those where fault throw is not visually identifiable to the interpreter in the profiles. Networks of planar features, reveal interconnected structures that may only have a few meters of throw, yet could play an equally important role in facilitating fluid migration.

## RESULTS AND INTERPRETATION

Although it is important that any description of brittle geological structures should start with the type of fault or fracture (e.g., Peacock and Sanderson, 2018), the resolution and quality of the seismic data commonly makes this impossible. For example, it is often not possible to resolve faults with throws of less than about 15 m (e.g., Pickering et al., 1997), strike–slip displacements may not create throws, and other types of structures can occur. Here, the minimum "most–resolvable" (i.e., >4 m) fault throw is 6 m (fault planes *29b, 14g, 8d*) found in the West–volume data set. Many of the fault planes extracted in the TEW–volume are smaller than the West–volume and not identified as faults, possibly because they have throws that are below the limit of resolution as explained above. The West–volume has a higher number (per unit area) of fault planes with throws well within data resolution (6–10 m) than those in the TEW–volume where only one fault plane exists with "most–resolvable" throw (15 m) (see Table 1), which is not explained by resolution differences, but by differences in the geologic structures in the two seismic volumes.

The high–resolution depth–converted 3D seismic volumes provide detailed structural information of the subsurface. Fault planes larger than ~3–4 m (in height) and ~6 m (in width) are effectively imaged in the 3D seismic data sets. The MLFL volume detects planar features marked by subtle bends and/or discontinuities in the reflections (almost not perceivable with the naked eye on the original seismic data) (Figure 5). These subtle discontinuities are often associated with structures indicating a throw of <3–4 m (vertical resolution). Here each MLFL extracted fault plane is categorized for effective interpretation of the structures (Table 1).

Notable differences exist between the east ("TEW–volume–(e)") and west ("TEW–volume–(w)") of the TEW–volume data set (Figure 6a). The fault planes, intersect multiple horizons in the TEW–volume–(e), indicating they have a larger surface area (Figure 4d). In the TEW–volume–(w) area, however, the fault planes intersect single horizons (i.e., B–3, O–4, and P–5) and have a smaller vertical extent (Figure 4c). By contrast, the vertical extent of fault planes in the West–volume data set, remains relatively consistent across both the "West–volume–(w)" and "West–volume–(e)" areas (Figures 4e, f).

**Fault and planar feature network characteristics**

The semi–automatic fault extraction reveals geometric differences between structures imaged at the TEW– and the West–volumes of the Vestnesa Ridge. The two seismic data sets have marginal differences in quality and resolution (differing in S/N ratio and by ~1 m vertical resolution at the seafloor) yet our approach provides meter–scale fault throw and planar feature interactions in both data sets and the interpretations have implications for the spatial and temporal evolution of sub seabed fluid migration in the region.

*TEW–volume*

There are four "fault zones" (FZ; defined in Appendix A, Table A–1) in the TEW survey, one in the central area (FZ1), and three fault zones in the east (FZ2–4) (Figure 6b), these probably having normal or oblique–normal displacements. FZ1 divides the TEW–volume into the TEW–volume–(w) and TEW–volume–(e) areas and is oriented approximately N–S. FZ2 and FZ3 both have ~NE–SW strike and FZ4 runs perpendicular to (i.e., ~NW–SE), and is bound by, FZ2 and FZ3. Rose plots were created using Allmendinger (2020) software to analyze the input planes. The length of the rose petals are scaled by area with 10° bin size. The analysis of 23 planes in the TEW–volume (see Supplementary Figure S–4) reveals a smaller average petal length (0.13), representing the occurrences of azimuth measurements per bin, than the West–volume (0.68), indicating a higher variability in fault orientation. The largest petal length is oriented ~NNW–SSE, in alignment with FZ1 and FZ4, while the smaller petal lengths are oriented ~NE–SW, in alignment with FZ2 and FZ3. Fault plane *10* (with ~15 m throw), and fault planes *1*, *5a*, *29c* in the TEW–volume (Figure 7d) have a strike range of 153–161°, which lies within the maximum value range of the rose diagram (17% of the population). An interpretation summary of the TEW–volume is provided (Appendix A, Table A–2).

*West–volume*

There are four fault zones (FZ5, FZ6, FZ7 and FZ8) in the West–volume (Figure 6d), these probably having normal or oblique–normal slip. FZ5 has the largest fault throw (~10 m) in the "West–volume–(e)" and shows elongated pockmarks at the surface (Figures 6d and 8f). FZ7

contains the largest faults in the "West–volume–(w)", with throws of up to 7 m. FZ6 and FZ8 are less well–defined, with throws that are at the lower limit of the resolution (e.g., fault planes *32b, 29c*). Some planar features found at the edge of the survey are imaged only in the attribute volumes and fault planes are not extracted, for example beneath the small, elongated pockmark "C–1" indicated in the West–volume–(w) (Figure 8f). Many of the fault planes exist below the deepest horizon (H3) towards the western flank of the Ridge (Figure 1f, Supplementary Figure S–3). We note that it is possible that these structures may be as young as the youngest sediments but may not have propagated to higher levels.

There are three distinct strike orientations: ~NW–SE, ENW–WSE, and ~E–W (Supplementary Figure S–5). The most prominent orientation is ~NW–SE, with a strike range of 151–160° (27% of the population) and similarly aligned to FZ5 and FZ6 (Figure 8d). Faults striking ~E–W (in approximate alignment with FZ7), are prominent in the west of the Vestnesa Ridge and also occur in the TEW–volume–(e) (e.g., fault planes *52a*, *61f*, *50b*) with a strike range of 78–92°. An interpretation summary of the West–volume is provided (Appendix A, Table A−3).

**Distribution of structures and fluid flow features**

Here, selected sets of interacting fault planes and isolated fault tips are identified in each volume (Figures 6b, d). Additional examples, illustrating common types of fault plane interactions within fault networks, defining types of fault plane interaction (such as abutting, stepping; Peacock et al., 2017) are provided (Supplementary Figure S–6). We compare the distribution of the interacting fault planes with the locations of fluid flow features, including pockmarks and gas chimneys (Figures 6b, d, 7e, 8f).

*Characterizing pockmarks and gas chimneys*

Pockmarks are key indicators of focused fluid flow and seepage and allow us to infer syn– and post–fault fluid migration (e.g., Waage et al., 2020). Pockmarks are prevalent across the two survey areas, both buried (i.e., paleo) and at the seafloor, with various sizes and shapes occurring. They are automatically extracted from the seafloor and from horizon H1, using a rule–based GIS methodology (Patton et al., 2015b; Cooke et al., 2023). Some seafloor pockmarks are more rounded, while many are elongated, oriented in the direction of the fault plane with which they are spatially related (see Supplementary Tables S–9 to S–13 and Figures S–7 to S–11 for pockmark characteristics). The more rounded pockmarks (~150 m diameter) may or may not be associated with the main fault zones (i.e., implying migration along or around faults) and could indicate fluid flow related to the BSR cross–cutting the dipping stratigraphy. These pockmarks appear in chains aligned with the bathymetric contours, indicating updip fluid migration (Figure 7e “arc”, discussed later).

In this study, gas chimneys are defined by whether the vertical seismic perturbation (i.e., characteristic of the chimney or fluid conduit) reaches the seafloor (i.e., they are “emergent”) or whether they stop at depth and fluid does not reach the seafloor (i.e., they are “blind”). Those that may have reached the seafloor in the past, and were then covered by sediments, are referred to as “buried”. The oldest blind chimney interpreted in this study persists for ~ 1 million years (FZ4) offering insight into the longevity of gas chimneys here and their influence on seismic data.

*Pockmarks and chimneys linked to fault plane interaction*

Most of the pockmarks are observed at the seafloor above fault plane segments and/or where two segments interact (Figures 6b, d, 7e, 8f, 9d, 10d). This indicates that most recent fluid flow activity occurred along or around the faults.

Pockmarks often occur at fault plane intersections, presumably where fluid is focused and possibly where pore pressure is higher and where dilation occurs (i.e., “dilational zones”; Gartrell et al., 2003). This implies that fault plane intersections are where the gas flow is channelized, long lived and/or rapid enough to create distinct chimneys and pockmarks (e.g., Gartrell et al., 2004; Ligtenberg, 2005; Michie and Braathen, 2024).

Seafloor pockmarks also commonly occur at a distance away from the mapped tips of fault planes, such as *4a, 29c* (Figures 6a, b, 7c–e). Note that the resolution limitation may result in the under–representation of the fault plane length (Figure 9c), so pockmarks may well occur at the actual tip of the fault plane rather than at the mapped tip.

Four fault plane segments along FZ6 illustrate the superposition of the structure (Figures 4, and 8a–f). The oldest fault plane segment (Y–1) is oriented NW–SE and interacts with the ~E–W striking younger fault plane (G–2), followed by an interaction with the youngest antithetic fault planes O–4 and P–5 (Figure 4a–b). The related group of fault planes provide an example of linkage between fault planes with different orientations, referred to here as fault profile irregularities by Ligtenberg (2005). Such fault profile irregularities may influence the development of weak locations in the fault zone (Ligtenberg, 2005). The imaging of such small irregularities would not be achieved in conventional (lower resolution) seismic.

A ~290 m wide x 620 m long fault–oriented pockmark occurs at the seafloor, with its maximum depth below sea level located at the end of fault plane *10g* at H3 (Figure 8e–f). Another example, illustrating structural evolution, occurs in the West–volume, between fault planes *14g*, *14c* and *15* (Figure 8a–f). The fault planes document a strike rotation through time, from ENE–WSW at the depth of horizons H3 and H2.25 to ~E–W at the depth of horizon H2. A ~90 m wide x 125 m long pockmark ("C–7") is present at the seafloor at the intersection of fault planes *14g* and *14c* (Figure 8e–f).

Seafloor pockmarks in the West–volume are largely restricted to the eastern section of the survey (e.g., West–volume–(e); Figure 6d) and appear to be spatially–related to fault planes. It is here that the BSR dips upwards and cross–cuts the stratigraphy, forming ~N–S oriented high amplitude ridges that appear as seismic artefacts. The fault planes identified as seismic artefacts, extending over the entire width of the survey, were excluded from the analysis. The seismic artefacts are visible in the fault likelihood volume horizon map (Figure 8e) at the lowermost horizon (H3), with high amplitude ridges striking parallel to FZ5 and FZ6.

*Pockmarks and chimneys related to BSR–ridges and BSR–highs*

Gas leakage and therefore pockmarks can occur without visible faults (e.g., Heggland, 2005). The seafloor pockmarks may not necessarily be attributed to fault zones but to locations of high pressure at the free–gas–gas hydrate interface (i.e., at the BSR) where migration can occur without fracturing (i.e., membrane seal failure; Bonto et al., 2021). Gas leakage tends to be concentrated where there are BSR–highs, or where the BSR cross–cuts the stratigraphy (i.e., BSR–ridges; Figure 11b–d). West of FZ1 in the TEW–volume, a series of approximately rounded seafloor pockmarks are aligned parallel to the bathymetry (Figures 6b and 7e). It is

interpreted that the chimneys identified here ("C–W1", "C–W2", "C–W3"; Figure 6b) might be formed by a different fluid flow mechanism, and not fracture–related (distinct from those exhibiting an elongated, fault–oriented morphology). Flow through sediments is probably caused by fluid pressures exceeding the capillary entry pressure, which does not promote fracturing.

There are fewer seafloor pockmarks (per unit area) in the West–volume than the TEW–volume, and the number of pockmarks associated with fault planes is proportionately greater (Appendix A, Table A–4). As mentioned earlier, there appears to be a spatial relationship between the fault zones (FZ5 and FZ6) and the BSR–ridges. Fluid migration associated with the BSR occurring at FZ5 and FZ6, is likely associated with fracturing and, the orientations of the fault planes are in alignment with the maximum azimuth (Supplementary Figure S–5). Also noted is that the pockmarks are in alignment with the isopach contour for the shallowing YP–3 sedimentary basin (Figure 1c). In addition, in the West–volume–(w), the pockmarks related to the fault planes (*14c, 14g* and *32b, 29c*) are considerably smaller here than the TEW–volume (Figures 7, 8).

*Chimney characteristics*

Examples of blind, buried, and emergent chimneys are observed between FZ2 and FZ3 in the TEW–volume (Figure 12) and between FZ7 and FZ8 in the West–volume (Figure 13). The variation in chimney geometries suggests interactions between the fault zones. A paleo pockmark with a diameter of ~300 m is present in the West–volume (Figure 13b), while the buried chimneys in the TEW–volume lack associated paleo pockmarks. In the West–volume, after the formation of the paleo pockmark (Figure 13, point "Y"), the buried chimney continued to develop upwards for approximately 0.6 million years (as estimated between horizons H2.25

and H1) before becoming blind (Figure 13c). The chimneys in both volumes exhibit changes in shape, with a wider and more rounded form near the lowermost horizon, transitioning to a narrower and elongated (or sometimes absent) form near the seafloor, suggesting variations in intensity through time or control by sediment properties that may be prone to fracturing. The emergent chimney "C–E2", in the TEW–volume, is wide beneath the BSR, narrows between horizons H2.25 and H1, then widens again at around H0.3, before narrowing once more between H0.3 and the seafloor (Figure 12b, c). Chimney "C–E2" is elongated in a NW–SE direction at the seafloor (Supplementary Figure S–7) and similarly, in the West–volume, chimney "C–1", becomes narrower and more elongated at the seafloor (Supplementary Figure S–9). Another observation is the reduction in size (width) of buried chimneys "C–3" and "C–4" as they approach the paleo pockmark at horizon H3 (Figure 13c). We interpret a re–widening of chimney "C–4" after the pockmark is buried at horizon H2.25 (Figure 13c). Additionally, fault–related chimneys may have experienced restricted flow. An example from the TEW–volume, shows blind chimneys between horizons H2.25 and H1 where paleo pockmarks are not visible (Figure 12, point "Y"). Alternatively, it is possible that paleo pockmarks were eroded, causing the chimneys to terminate at unconformities where pockmarks have been removed.

## DISCUSSION

The method employed in this study has uncovered details in the seismic data sets that have improved the analyses of interconnected fault/planar structures and fluid flow features. Seismic data have been used in other regions to identify structures related to fluid flow (e.g., Ligtenberg 2005; Moss and Cartwright, 2010; Cartwright and Santamarina, 2015) but rarely using high–resolution data in the near–surface.

The interaction of low displacement structures imaged in the fault likelihood volume (Figures 7 and 8) within or around the fault zones may be responsible for controlling fluid flow seepage. There are, however, limits to what we can see in seismic data and interpretations of fault interaction are largely inferred. We use the term "distributed gas leakage zone" (defined in Appendix A, Table A–1), introduced here, based on the term "distributed fault damage zone" where deformation is more intense than the region background level (e.g., Kim et al., 2004; McGinnis et al., 2016; Peacock et al., 2017). Distributed fault damage may be below the resolution of the seismic data set, with activity only marked by gas chimneys (i.e., distributed gas leakage zone; Supplementary Figure S–10). Relatively high densities of fault planes exist in each MLFL volume, supporting the idea that there is a relationship between distributed gas leakage and distributed damage zones. Two possible distributed gas leakage zones are identified in this study based on clusters of gas chimneys between the fault zones (Figures 9, 10, Appendix B, Table B–1).

Fault damage zones associated with "transfer zones" (defined in Appendix A, Table A–1) have been shown to influence fluid flow (e.g., Fossen and Hurich, 2005; Rotevatn et al., 2007). Evidence for fluid flow in a zone of gas leakage is observed in the breached transfer zone (i.e. FZ4; Figure 9). A pattern of faults and planar features, referred to as "box–faults" (Griffiths, 1980; defined in Appendix A, Table A–1), is most distinctly seen at the horizons corresponding to the sedimentary layers dated between ~1 to 0.4 Ma (Figures 7 and 9). Fault planes *1* and *5a* are examples of structures interpreted as partially imaged box–faults within the transfer zone (Figure 11b). These fault planes illustrate "unresolved" structures classified as planar features. Fault planes *1* and *5a* are just about detectable in the shallowest horizon (H0.3) extraction

(Figure 9a) and associated planar features in the breaching transfer zone are imaged most clearly in the deeper horizons (H2, H2.25; Figure 9).

"Deformation bands" (defined in Appendix A, Table A–1) could have developed within distributed gas leakage zones, though it is not possible to prove in seismic data. They can act as conduits or baffles to fluid flow (e.g., Fossen and Bale, 2007; Kolyukhin et al., 2010; Michie and Braathen, 2023) and joints may develop in carbonate–cemented sediments (Barnicoat et al., 2009). Methane–derived authigenic carbonates found in the study area (dated to ~20–5 Ka, ~50–40 Ka and ~160–133 Ka; Himmler et al., 2019) are proposed at deformed intervals (i.e., at ~130 Ka and probably deeper, at ~1 Ma; Cooke et al., 2023). Joint formation in carbonate–rich sediments, results in high permeability fracture networks (Barnicoat et al., 2009), which may be expressed in the seismic by chimney widening (Figure 12c, see Appendix B "Venting periods linked to glacial cycles" for further details).

Stratigraphic layering (e.g., Smart et al., 2023) can control the type of damage around faults, and fluids might be dispersed away via thief layers (Barnicoat et al., 2009). Layers containing clay–rich sediments can behave in a ductile way during burial and form effective seals (e.g., Downey, 1984), leading to overpressured fluid compartments. Such conditions may develop where there is an abrupt change in lithology, for example at the boundary between a thick fine–grained interbed and thin layers of sand, with different layers having differing coefficients of internal friction (e.g., Downey, 1984). The clay seal units could be breached episodically and form overpressure in overlying sediments, resulting in structures such as pseudo–diapirs (which must be distinguished from typical shale diapirism, i.e., deep–seated shales). Pseudo–diapirs form when shales start to move at near–surface depth almost

immediately after deposition (Magara, 1978), and they are relatively soft and mobile, separated by intervals of non–extruded sediments. We use the term “honeycomb” to describe the inferred hexagonal pattern created by the mobilization of sediment captured in higher–resolution seismic data in the TEW–volume (Figure 9a). The pattern indicates an undulating surface of small (<20–50 m width and ~3–5 m in the vertical) fluid flow features, interpreted as buried pockmarks, carbonate mounds and/or overpressured features, possibly related to faults that are below the resolution of the data set.

After the extraction of fault planes with meter–scale throws, we can observe the superposition of faults and planar structures to determine their sequence of development. When fault segments get close enough, they start to interact (e.g., Fossen and Rotevatn, 2016). Zones of fault interaction can occur on scales of millimeters to tens of km, with strain or displacement being transferred from one fault to another (e.g., Larsen, 1988; Fossen and Rotevatn, 2016). Geometries and displacement profiles can be used to determine fault interaction (e.g., Peacock and Sanderson, 1991), but the displacements are too small in the study area, so fault interaction is inferred based on gas leakage.

Fluid flow is linked to pressurized free gas beneath the BSR (marking the base of the gas hydrate stability zone). The BSR mostly runs parallel to the seafloor and can cross–cut the seismic stratigraphy. Chimneys and pipes form above places where the BSR is found to cross–cut the seismic stratigraphy. The volume of gas that builds up beneath the BSR generally varies along the base of the gas hydrate stability zone, influenced by spatial changes in geothermal gradient and both lateral and vertical changes of gas compositions and concentrations (e.g., Plaza–Faverola et al., 2017; Singhroha et al., 2019). Emergent chimneys and fault–oriented

pockmarks exist where the BSR cross–cuts the stratigraphic layers (e.g., FZ5 and FZ6), forming a deformation ridge or front that lies parallel to the fault zones. We suggest that there is a relationship between the BSR and fault planes relating to the breached transfer zone (see Appendix B, Table B–1). Lastly, significant phase–reversed high amplitude reflections are documented in the seismic at locations where the BSR intersects with dipping stratigraphy, downdip of the BSR–high. Pipes frequently occur above these BSR–cross–cutting zones (Figure 11d), consistent with observations of overpressure–driven leakage in petroleum systems (e.g., Foschi and Cartwright, 2020). These findings emphasize the intricate relationship between geologic structures and fluid migration, providing valuable insights for understanding both natural gas hydrate and petroleum systems.

## CONCLUSIONS

A pre–trained fault prediction machine learning model is tested on two high–resolution 3D seismic data sets. The process is semi–automated, meaning that the automatically extracted fault planes for each volume are selected based on their age and on whether there is a visible throw (i.e., a fault) or not (i.e., planar feature). Many of the faults recorded are close to the limit of seismic resolution, with it not being possible to measure throws below ~3–4 m. The planar features may be faults, as indicated by curvature and subtle discontinuities in the seismic reflections.

The two data sets reveal small differences in quality and resolution, thereby influencing the imaging of structures and fluid flow features. Despite these differences, both data sets were interpreted and compared, with an emphasis on: (1) fault interaction and deformation associated

with fault zones; (2) gas chimney classification; and (3) the influence of the BSR on the formation of faults/planar features, and fluid flow. The main results are as follows:

- Channelized fluid flow and the formation of gas chimneys appear to be controlled by fault interaction and linkage, which are interpreted to have created networks of planar features and dilational zones. Pockmarks commonly occur at fault intersections or at the tips of faults.
- The faults that were once fluid migration pathways, by evidence of seafloor pockmarks and emergent paleo gas chimneys, have become sealed because there being no evidence of present–day gas release in the study areas. Paleo gas chimneys studied within the distributed gas leakage zones indicate where fluid flow was released in the past (i.e., buried/eroded pockmarks), and when fluid did not emerge at the paleo seafloor (i.e., blind chimneys).
- It is not possible to extract all the planar features using the method outlined in this paper because many will be below the seismic resolution. Those that fall below the resolution limits of the seismic data sets (~3–4 m) and are too small to be automatically extracted, are observed only in map view as high likelihood in the machine learning fault likelihood and semblance volume horizons.
- Some gas leakage may have occurred at locations above the BSR–ridges (i.e., where the BSR cross–cuts the dipping stratigraphy) and at BSR–highs (i.e., in places of shallowest burial of the BSR), rather than at fault plane intersections. Free gas is concentrated in such areas where there is alignment with the Ridge bathymetry and/or the YP–3 contours.

The method outlined in this work offers significant advantages in understanding gas leakage, particularly when high–resolution seismic data are available and where leakage is controlled by faults with throws of only a few meters. The approach improves the extraction of faults with meter–scale throws and networks of planar features, using advanced imaging techniques, otherwise overlooked in manual seismic interpretation. The level of detail is crucial when assessing potential gas leakage pathways as even minor faults can act as conduits for gas migration. Our analyses provide new insights into gas leakage and suggest that even fault networks with sub–meter displacements are likely to play an important role in fluid migration in the subsurface.

## ACKNOWLEDGMENTS

This work is part of the SEAMSTRESS project, supported by grants from the Tromsø Research Foundation (project nr. A31680) and the Research Council of Norway (project nr. 287865). The work has been conducted under the Norwegian Centers of Excellence CAGE Centre for Arctic Gas Hydrate, Environment and Climate (Project nr. 223259) and currently iC3 Centre for ice, Cryosphere, Carbon and Climate (project nr. 332635). We are grateful to the ship and scientific crew on board R/V Helmer Hanssen for the seismic data acquisition. We thank OpendTect for software and support. FC is particularly grateful to Rosalind King for help and advice with stereonets. We thank the reviewers for their valuable feedback and suggestions, which have significantly enhanced the quality of this manuscript.

Supplementary **Figures S–1 to S–11** and **Tables S–1 to S–13** can be found in the supporting information.

APPENDIX A



APPENDIX B



**Venting periods linked to glacial cycles**

The variations in chimney width observed at distinct intervals appear to align with and precede major venting periods at ~0.2 Ma, and ~0.4 Ma, documented from the mid–Norwegian margin and suggested to be associated with glacial–interglacial transitions (Plaza–Faverola et al., 2011), where fracture density is recorded as high (Cooke et al., 2023). A link between major methane seepage events before and after 130 Ka and glacial cycles is also inferred from integrated data analyses in the South China Sea (Deng et al., 2021).

The venting period occurring between ~1.5 Ma (H3) and ~0.4 Ma (H2) might have been substantial enough to deplete the gas in the volumes studied here. Consequently, the replenishment of gas may not have been sufficient for the chimney to remain active, leaving behind upward domed remobilized sediments (Figure 13b). Gas may be depleted below the buried chimneys but actively charged for the emergent chimneys that have continued above ~0.2 Ma (H1) and have reached the present–day seafloor (i.e., Figures 12 and 13).

## REFERENCES

Acuña-Uribe, M., M. C. Pico-Forero, P. Goyes-Peñafiel, and D. Mateus, 2021, Enhanced ant tracking: Using a multispectral seismic attribute workflow to improve 3D fault detection: The Leading Edge, **40**, 502–512, doi.org/10.1190/tle40070502.1.

AlBinHassan, N. M., Y. Luo, and M. N. Al-Faraj, 2006, 3D edge-preserving smoothing and applications: Geophysics, **71**, P5–P11, doi.org/10.1190/1.2213050.

Alexandropoulou, N., M. Winsborrow, K. Andreassen, A. Plaza-Faverola, P.-A. Dessandier, R. Mattingsdal, N. Baeten, and J. Knies, 2021, A continuous seismostratigraphic framework for the Western Svalbard-Barents Sea Margin over the last 2.7 Ma: Implications for the Late Cenozoic glacial history of the Svalbard-Barents Sea Ice Sheet: Frontiers in Earth Science, **9**, 656732.

Allmendinger, R. W., N. Cardozo, and D. M. Fisher, 2011, Structural Geology Algorithms: Vectors and Tensors: Cambridge University Press, doi.org/10.1017/CBO9780511920202.

An, Y., J. Guo, Q. Ye, C. Childs, J. Walsh, and R. Dong, 2021, Deep convolutional neural network for automatic fault recognition from 3D seismic datasets: Computers & Geosciences, **153**, 104776, doi.org/10.1016/j.cageo.2021.104776.

Anderson, E. M., 1905, The Dynamics of Faulting: Transactions of the Edinburgh Geological Society, **8**, 387–402, doi.org/10.1144/transed.8.3.387.

Auguy, C., G. Calvès, Y. Calderon, and S. Brusset, 2017, Seismic evidence of gas hydrates, multiple BSRs and fluid flow offshore Tumbes Basin, Peru: Marine Geophysical Research, **38**, 409-423, doi.org/10.1007/s11001-017-9319-2.

Bahorich, M. S., and S. L. Farmer, 1995, 3D seismic discontinuity for faults and stratigraphic features: The coherence cube, SEG Technical Program Expanded Abstracts, SEG, 93–96, doi.org/10.1190/1.1887523.

Barnicoat, A. C., H. A. Sheldon, and A. Ord, 2009, Faulting and fluid flow in porous rocks and sediments: Implications for mineralisation and other processes: Mineralium Deposita, **44**, 705–718, doi.org/10.1007/s00126-009-0236-4.

Bond, C. E., 2015, Uncertainty in structural interpretation: Lessons to be learnt: Journal of Structural Geology, **74**, 185–200, doi.org/10.1016/j.jsg.2015.03.003.

Bond, C. E., A. D. Gibbs, Z. K. Shipton, and S. Jones, 2007, What do you think this is? "Conceptual uncertainty" in geoscience interpretation: GSA Today, **17**, 4-10, doi.org/10.1130/GSAT01711A.1.

Bonto, M., M.J. Welch, M. Lüthje, S.I. Andersen, M.J. Veshareh, F. Amour, A. Afrough, R. Mokhtari, M.R. Hajiabadi, M.R. Alizadeh, C.N. Larsen, and H.M. Nick, 2021, Challenges and enablers for large-scale CO2 storage in chalk formations: Earth-Science Reviews, **222**, 103826, doi.org/10.1016/j.earscirev.2021.103826.

Bosworth, W., 2024, Continental rift asymmetry and segmentation – contributions from the African plate: Journal of African Earth Sciences, **210**, 105128, doi.org/10.1016/j.jafrearsci.2023.105128.

Breivik, A. J., J. Verhoef, and J. I. Faleide, 1999, Effect of thermal contrasts on gravity modeling at passive margins: Results from the western Barents Sea: Journal of Geophysical Research: Solid Earth, **104**, 15293–15311, doi.org/10.1029/1998JB900022.

Bünz, S., 2022, Cruise CAGE-18-4. CAGE – Centre for Arctic Gas Hydrate: Environment and Climate Report Series 6, doi.org/10.7557/cage.6850.

Bünz, S., S. Polyanov, S. Vadakkepuliyambatta, C. Consolaro, and J. Mienert, 2012, Active gas venting through hydrate-bearing sediments on the Vestnesa Ridge, offshore W-Svalbard: Marine Geology, **332–334**, 189–197, doi.org/10.1016/j.margeo.2012.09.012.

Cartwright, J., and C. Santamarina, 2015, Seismic characteristics of fluid escape pipes in sedimentary basins: Implications for pipe genesis: Marine and Petroleum Geology, **65**, 126-140 doi.org/10.1016/j.marpetgeo.2015.03.023.

Chen, H., D. Tang, Y. Liu, H. Gu, and C. Zhou, 2022, Augmented deep learning workflow for robust fault prediction over multiple tectonic regimes: Journal of Geophysics and Engineering, **19**, 914–926, doi.org/10.1093/jge/gxac056.

Chopra, S., and K. J. Marfurt, 2013, Preconditioning seismic data with 5D interpolation for computing geometric attributes: SEG Technical Program Expanded Abstracts, SEG, 1368–1373, doi.org/10.1190/segam2013-0169.1.

Consolaro, C., T. L. Rasmussen, G. Panieri, J. Mienert, S. Bünz, and K. Sztybor, 2015, Carbon isotope (δ 13 C) excursions suggest times of major methane release during the last 14 kyr

in Fram Strait, the deep-water gateway to the Arctic: Climate of the Past, **11**, 669–685, doi.org/10.5194/cp-11-669-2015.

Cooke, F., A. Plaza-Faverola, S. Bünz, N. Sultan, H. Ramachandran, H. Bedle, H. Patton, S. Singhroha, and J. Knies, 2023, Sedimentary deformation relating to episodic seepage in the last 1.2 million years: A multi-scale seismic study from the Vestnesa Ridge, eastern Fram Strait: Frontiers in Earth Science, **11**, 1188737, doi.org/10.3389/feart.2023.1188737.

Crane, K., H. Doss, P. Vogt, E. Sundvor, G. Cherkashov, I. Poroshina, and D. Joseph, 2001, The role of the Spitsbergen shear zone in determining morphology, segmentation and evolution of the Knipovich Ridge: Marine Geophysical Researches, **22**, 153–205, doi.org/10.1023/A:1012288309435.

Crutchley, G. J., C. Berndt, D. Klaeschen, and D. G. Masson, 2011, Insights into active deformation in the Gulf of Cadiz from new 3-D seismic and high-resolution bathymetry data: Geochemistry, Geophysics, Geosystems, **12**, Q07016, doi.org/10.1029/2011GC003576.

Deng Y., F. Chen, Q. Guo, Y. Hu, D. Chen, S. Yang, J. Cao, H. Chen, R. Wei, S. Cheng, J. Zhou, C. Liu, X. Jiang, and J. Zhu, 2021, Possible links between methane seepages and glacial-interglacial transitions in the south China Sea: Geophysics Research Letters **48**, e2020GL091429, doi.org/10.1029/2020GL091429.

Dessandier, P.-A., J. Knies, A. Plaza-Faverola, C. Labrousse, M. Renoult, and G. Panieri, 2021, Ice-sheet melt drove methane emissions in the Arctic during the last two interglacials: Geology, **49**, 799-803, doi.org/10.1130/G48580.1.

Di, H., Z. Wang, and G. Al Regib, 2018, Deep convolutional neural networks for seismic salt-body delineation: Presented at the 2018 American Association of Petroleum Geologists

Annual Convention & Exhibition, American Association of Petroleum Geologists, doi.org/10.1306/70630Di2018.

Downey, M. W., 1984, Evaluating seals for hydrocarbon accumulations: American Association of Petroleum Geologists Bulletin, **68**, 1752-1763, doi.org/10.1306/AD461994-16F7-11D7-8645000102C1865D.

Dumais, M.-A., L. Gernigon, O. Olesen, S. E. Johansen, and M. Brönner, 2020, New interpretation of the spreading evolution of the Knipovich Ridge derived from aeromagnetic data: Geophysical Journal International, **224**, 1422–1428, doi.org/10.1093/gji/ggaa527.

Eiken, O., and K. Hinz, 1993, Contourites in the Fram Strait: Sedimentary Geology, **82**, 15–32, doi.org/10.1016/0037-0738(93)90110-Q.

Faleide, T. S., A. Braathen, I. Lecomte, M. J. Mulrooney, I. Midtkandal, A. J. Bugge, and S. Planke, 2021, Impacts of seismic resolution on fault interpretation: Insights from seismic modelling: Tectonophysics, **816**, 229008, doi.org/10.1016/j.tecto.2021.229008.

Foschi, M., and J. A. Cartwright, 2020, Seal failure assessment of a major gas field via integration of seal properties and leakage phenomena: American Association of Petroleum Geologists Bulletin, **104**, 1627–1648, doi.org/10.1306/02282018111.

Fossen, H., and C. A. Hurich, 2005, The Hardangerfjord Shear Zone in SW Norway and the North Sea: A large-scale low-angle shear zone in the Caledonian crust: Journal of the Geological Society, **162**, 675–687, doi.org/10.1144/0016-764904-136.

Fossen, H., and A. Bale, 2007, Deformation bands and their influence on fluid flow: American Association of Petroleum Geologists Bulletin, **91**, 1685–1700, doi.org/10.1306/07300706146.

Fossen, H., 2010, Structural Geology, 2nd edition, Chapter 8: Cambridge University Press.

Fossen, H., and A. Rotevatn, 2016, Fault linkage and relay structures in extensional settings—A review: Earth-Science Reviews, **154**, 14–28, doi.org/10.1016/j.earscirev.2015.11.014.

Freeman, B., P. J. Boult, G. Yielding, and S. Menpes, 2010, Using empirical geological rules to reduce structural uncertainty in seismic interpretation of faults: Journal of Structural Geology, **32**, 1668–1676, doi: 10.1016/j.jsg .2009.11.001.

Gao, H., X. Wu, and G. Liu, 2021, ChannelSeg3D: Channel simulation and deep learning for channel interpretation in 3D seismic images: Geophysics, **86**, IM73–IM83, doi.org/10.1190/geo2020-0572.1.

Gartrell, A., Y. Zhang, M. Lisk, and D. Dewhurst, 2003, Enhanced hydrocarbon leakage at fault intersections: An example from the Timor Sea, Northwest Shelf, Australia: Journal of Geochemical Exploration, Proceedings of Geofluids IV, **78–79**, 361–365, doi.org/10.1016/S0375-6742(03)00125-0.

Gibbs, A. D., 1984, Structural evolution of extensional basin margins: Journal of the Geological Society, **141**, 609–620, doi.org/10.1144/gsjgs.141.4.0609.

Godefroy, G., G. Caumon, M. Ford, G. Laurent, and C. A.-L. Jackson, 2018, A parametric fault displacement model to introduce kinematic control into modeling faults from sparse data: Interpretation, **6**, B1–B13, doi.org/10.1190/INT-2017-0059.1.

Goswami, B. K., K. A. Weitemeyer, T. A. Minshull, M. C. Sinha, G. K. Westbrook, A. Chabert, T. J. Henstock, S. Ker, 2015, A joint electromagnetic and seismic study of an active pockmark within the hydrate stability field at the Vestnesa Ridge, West Svalbard margin: Journal of Geophysical Research: Solid Earth, **120**, 6797–6822, doi.org/10.1002/2015JB012344.

Griffiths, P. S., 1980, Box-fault systems and ramps: Atypical associations of structures from the eastern shoulder of the Kenya Rift: Geological Magazine, **117**, 579–586, doi.org/10.1017/S0016756800028910.

Groot, P. de., M. Pelissier, H. Refayee, and M. van Hout, 2021, Deep Learning Seismic Object Detection Examples: DEW Journal, **30**, 31-36.

Groot, P. de., M. van Hout, and H. Refayee, 2023, How Machine Learning saves time and costs in subsurface interpretation studies: DEW Journal, **42**, 29-36.

Hale, D., 2013, Methods to compute fault images, extract fault surfaces, and estimate fault throws from 3D seismic images: Geophysics, **78**, 1MA-Z51, doi.org/10.1190/geo2012-0331.1.

Heggland, R., 2005, Using gas chimneys in seal integrity analysis: A discussion based on case histories, *in* P. Boult and J. Kaldi, eds., Evaluating fault and cap rock seals: American Association of Petroleum Geologists Hedberg Series 2, 237–245.

Himmler, T., D. Sahy, T. Martma, G. Bohrmann, A. Plaza-Faverola, S. Bünz, D. J. Condon, J. Knies, and A. Lepland, 2019, A 160,000-year-old history of tectonically controlled methane seepage in the Arctic: Science Advances, **5**, eaaw1450, doi.org/10.1126/sciadv.aaw1450.

Howe, J. A., T. M. Shimmield, R. Harland, and N. Eyles, 2008, Late Quaternary contourites and glaciomarine sedimentation in the Fram Strait: Sedimentology, **55**, 179–200, doi.org/10.1111/j.1365-3091.2007.00897.x.

Hustoft, S., S. Bünz, J. Mienert, and S. Chand, 2009, Gas hydrate reservoir and active methane-venting province in sediments on <20 Ma young oceanic crust in the Fram Strait, offshore

NW-Svalbard: Earth and Planetary Science Letters, **284**, 12–24, doi.org/10.1016/j.epsl.2009.03.038.

Jessen, S. P., T. L. Rasmussen, T. Nielsen, and A. Solheim, 2010, A new Late Weichselian and Holocene marine chronology for the western Svalbard slope 30,000–0 cal years BP: Quaternary Science Reviews, **29**, 1301–1312, doi.org/10.1016/j.quascirev.2010.02.020.

Kamb, W. B., 1959, Ice petrofabric observations from Blue Glacier, Washington in relation to theory and experiment: Journal of Geophysical Research, **64**, 1891– 1909.

Kim, Y. S., D. C. P. Peacock, and D. J. Sanderson, 2004, Fault damage zones: Journal of Structural Geology, **26**, 503–517, doi.org/10.1016/j.jsg.2003.08.002.

Knies, J., M. Daszinnies, A. Plaza-Faverola, S. Chand, Ø. Sylta, S. Bünz, J. E. Johnson, R. Mattingsdal, and J. Mienert, 2018, Modelling persistent methane seepage offshore western Svalbard since early Pleistocene: Marine and Petroleum Geology, **91**, 800–811, doi.org/10.1016/j.marpetgeo.2018.01.020.

Knipe, R. J., G. Jones, and Q. J. Fisher, 1998, Faulting, fault sealing and fluid flow in hydrocarbon reservoirs: an introduction, *in* G. Jones, Q. J. Fisher, and R. J. Knipe, eds., Faulting, Fault Sealing and Fluid Flow in Hydrocarbon Reservoirs: Geological Society 147, vii–xxi, doi.org/10.1144/GSL.SP.1998.147.01.01.

Kolyukhin, D., S. Schueller, M. S. Espedal, and H. Fossen, 2010, Deformation band populations in fault damage zone—impact on fluid flow: Computational Geosciences, **14**, 231–248, doi.org/10.1007/s10596-009-9148-8.

Larsen, P.-H., 1988, Relay structures in a Lower Permian basement-involved extension system, East Greenland: Journal of Structural Geology, **10**, 3–8, doi.org/10.1016/0191-8141(88)90122-8.

Li, S., C. Yang, H. Sun, and H. Zhang, 2019, Seismic fault detection using an encoder–decoder convolutional neural network with a small training set: Journal of Geophysics and Engineering, **16**, 175–189, doi.org/10.1093/jge/gxy015.

Ligtenberg, J. H., 2005, Detection of fluid migration pathways in seismic data: Implications for fault seal analysis: Basin Research, **17**, 141–153, doi.org/10.1111/j.1365-2117.2005.00258.x.

Lisle, R. J., 1994, Detection of zones of abnormal strains in structures using Gaussian curvature analysis: American Association of Petroleum Geologists Bulletin, **78**, 1811-1819.

Long, J. J., and J. Imber, 2011, Geological controls on fault relay zone scaling: Journal of Structural Geology, **33**, 1790-1800, doi.org/10.1016/j.jsg.2011.09.011.

Luo, Y., M. Marhoon, S. Al Dossary, and M. Al-faraj, 2002, Edge-preserving smoothing and applications: The Leading Edge, **21**, 136–158, doi.org/10.1190/1.1452603.

Magara, K., 1978, Importance of abnormal pressuring in shale diapirism, *in* K. Magara, ed., Compaction and Fluid Migration Practical Petroleum Geology: Developments in Petroleum Science 9, 243-256.

Marfurt, K. J., V. Sudhaker, A. Gersztenkorn, K. D. Crawford, and S. E. Nissen, 1999, Coherency calculations in the presence of structural dip: Geophysics **64**, 104–111, doi.org/10.1190/1.1444508.

Marsset, T., B. Marsset, S. Ker, Y. Thomas, and Y. Le Gall, 2010, High and very high resolution deep-towed seismic system: Performance and examples from deep water Geohazard studies, Deep Sea Research Part I: Oceanographic Research Papers, **57**, 628–637, doi.org/10.1016/j.dsr.2010.01.001.

Mattingsdal, R., J. Knies, K. Andreassen, K. Fabian, K. Husum, K. Grøsfjeld, and S. de Schepper, 2014, A new 6 Myr stratigraphic framework for the Atlantic–Arctic Gateway: Quaternary Science Reviews, **92**, 170–178, doi.org/10.1016/j.quascirev.2013.08.022.

McGinnis, R. N., D. A. Ferrill, A. P. Morris, and K. J. Smart, 2016, Insight on mechanical stratigraphy and subsurface interpretation, *in* B. Krantz, C. Ormand, and B. Freeman eds., 3-D Structural Interpretation: Earth, Mind, and Machine: American Association of Petroleum Geologists 111, doi.org/10.1306/13561989M1113673.

Michie, E. A. H., and A. Braathen, 2024, How displacement analysis may aid fault risking strategies for $CO_2$ storage: Basin Research, **36**, e12807, doi.org/10.1111/bre.12807.

Morley, C. K., R. A. Nelson, T. L. Patton, and S. G. Munn, 1990. Transfer zones in the East African rift system and their relevance to hydrocarbon exploration in rifts: Bulletin of the American Association of Petroleum Geologists **74**, 1234-1253.

Moss, J. L., and J. Cartwright, 2010, The spatial and temporal distribution of pipe formation offshore Namibia: Marine and Petroleum Geology, **27**, 1216-1234, doi.org/10.1016/j.marpetgeo.2009.12.013.

Nixon, C. W., D. J. Sanderson, S. J. Dee, J. M. Bull, R. J. Humphreys, and M. H. Swanson, 2014, Fault interactions and reactivation within a normal-fault network at Milne Point, Alaska: American Association of Petroleum Geologists Bulletin, **98**, 2081–2107, doi.org/10.1306/04301413177.

Osti, G., K. A. Waghorn, M. Waage, A. Plaza-Faverola, and B. Ferré, 2019, Evolution of contourite drifts in regions of slope failures at eastern Fram Strait: Arktos, **5**, 105–120, doi.org/10.1007/s41063-019-00070-y.

Patton, H., K. Andreassen, L. R. Bjarnadóttir, J. A. Dowdeswell, M. C. M. Winsborrow, R. Noormets, L. Polyak, A. Auriac, and A. Hubbard, 2015a, Geophysical constraints on the dynamics and retreat of the Barents Sea ice sheet as a paleobenchmark for models of marine ice sheet deglaciation: Reviews Geophysics, **53**, 1051–1098, doi.org/10.1002/2015RG000495.

Patton, H., D. A. Swift, C. D. Clark, S. J. Livingstone, S. J. Cook, and A. Hubbard, 2015b, Automated mapping of glacial overdeepenings beneath contemporary ice sheets: Approaches and potential applications: Geomorphology, **232**, 209–223, doi.org/10.1016/j.geomorph.2015.01.003.

Peacock, D. C. P., and D. J. Sanderson, 1991, Displacements, segment linkage and relay ramps in normal fault zones: Journal of Structural Geology, **13**, 721–733, doi.org/10.1016/0191-8141(91)90033-F.

Peacock, D. C. P., and D. J. Sanderson, 2018, Structural analyses and fracture network characterisation: Seven pillars of wisdom: Earth-Science Reviews, **184**, 13–2, doi.org/10.1016/j.earscirev.2018.06.006.

Peacock, D. C. P., R. Knipe, and D. Sanderson, 2000, Glossary of normal faults: Journal of Structural Geology, **22**, 291–305, doi.org/10.1016/S0191-8141(00)80102-9.

Peacock, D. C. P., C. W. Nixon, A. Rotevatn, D. J. Sanderson, and L. F. Zuluaga, 2016, Glossary of fault and other fracture networks: Journal of Structural Geology, **92**, 12–29, doi.org/10.1016/j.jsg.2016.09.008.

Peacock, D. C. P., C. W. Nixon, A. Rotevatn, D. J. Sanderson, and L. F. Zuluaga, 2017, Interacting faults: Journal of Structural Geology, **97**, 1–22, doi.org/10.1016/j.jsg.2017.02.008.

Pedersen, S. I., T. Randen, L. Sønneland, and Ø. Steen, 2002, Automatic fault extraction using artificial ants: Presented at the 2002 SEG International Exposition and 72nd Annual Meeting SEG-2002-0512.

Petersen, C. J., S. Bünz, S. Hustoft, J. Mienert, and D. Klaeschen, 2010, High-resolution P-cable 3D seismic imaging of gas chimney structures in gas hydrated sediments of an Arctic sediment drift: Marine and Petroleum Geology, **27**, 1981–1994, doi.org/10.1016/j.marpetgeo.2010.06.006.

Pickering, G., D. C. P. Peacock, D. J. Sanderson, and J. M. Bull, 1997, Modelling tip zones to predict the displacement and length characteristics of faults: American Association of Petroleum Geologists Bulletin, **81**, 82-99, doi.org/10.1306/522B4299-1727-11D7-8645000102C1865D.

Planke, S., F. N. Erikson, C. Berndt, J. Mienert, and D. Masson, 2009, P-cable high-resolution seismic: Oceanography, **22**, 85–85, doi.org/10.5670/oceanog.2009.09.

Plaza-Faverola, A., S. Bünz, and J. Mienert, 2011, Repeated fluid expulsion through sub-seabed chimneys offshore Norway in response to glacial cycles: Earth and Planetary Science Letters, **305**, 297–308, doi.org/10.1016/j.epsl.2011.03.001.

Plaza-Faverola, A., S. Bünz, J. E. Johnson, S. Chand, J. Knies, J. Mienert, and P. Franek, 2015, Role of tectonic stress in seepage evolution along the gas hydrate-charged Vestnesa Ridge, Fram Strait: Arctic seepage modulated by tectonics: Geophysical Research Letters, **42**, 733–742, doi.org/10.1002/2014GL062474.

Plaza-Faverola, A., S. Vadakkepuliyambatta, W.-L. Hong, J. Mienert, S. Bünz, S. Chand, and J. Greinert, 2017, Bottom-simulating reflector dynamics at Arctic thermogenic gas provinces:

An example from Vestnesa Ridge, offshore west Svalbard: Journal of Geophysical Research: Solid Earth, **122**, 4089–4105, doi.org/10.1002/2016JB01376.

Plaza-Faverola, A., N. Sultan, R. G. Lucchi, N. El bani Altuna, H. Ramachandran, S. Singhroha, F. Cooke, S. Vadakkepuliyambatta, M. M. Ezat, and T. L. Rasmussen, 2023, Spatial changes in gas transport and sediment stiffness influenced by regional stress: Observations from piezometer data along Vestnesa Ridge, Eastern Fram Strait: Journal of Geophysical Research: Solid Earth, **128**, e2022JB025868, doi.org/10.1029/2022JB025868.

Powers, M. C., 1967, Fluid-release mechanisms in compacting marine mudrocks and their importance in oil exploration: American Association of Petroleum Geologists Bulletin, **51**, 1240-1254, doi.org/10.1306/5D25C137-16C1-11D7-8645000102C1865D.

Price, N.J., 1966. Fault and Joint Development in Brittle and Semi-Brittle Rock: Pergamon, Oxford.

Reches, Z., and D. A. Lockner, 1994, Nucleation and growth of faults in brittle rocks: Journal of Geophysical Research: Solid Earth, **99**, 18159–18173, doi.org/10.1029/94JB00115.

Ritzmann, O., W. Jokat, W. Czuba, A. Guterch, R. Mjelde, and Y. Nishimura, 2004, A deep seismic transect from Hovgård Ridge to northwestern Svalbard across the continental-ocean transition: A sheared margin study: Geophysical Journal International, **157**, 683–702, doi.org/10.1111/j.1365-246X.2004.02204.x.

Roberts, A., 2001, Curvature attributes and their application to 3D interpreted horizons: First Break, **19**, 85–100, doi.org/10.1046/j.0263-5046.2001.00142.x.

Ronneberger, O., P. Fischer, and T. Brox, 2015, U-Net: Convolutional networks for biomedical image segmentation, *in* N. Navab, J. Hornegger, W. M. Wells, and A. F. Frangi, eds.,

Medical Image Computing and Computer-Assisted Intervention – MICCAI 2015: Lecture Notes in Computer Science 9351, 234–241, doi.org/10.1007/978-3-319-24574-4_28.

Rotevatn, A., H. Fossen, J. Hesthammer, T. E. Aas, and J. A. Howell, 2007, Are relay ramps conduits for fluid flow? Structural analysis of a relay ramp in Arches National Park, Utah, *in* L. Lonergan, D. J. Sanderson, R. J. H. Jolly, and K. Rawnsley eds., Fractured Reservoirs: Geological Society 270, 55–71, doi.org/10.1144/GSL.SP.2007.270.01.04.

Scholz, C. H., and P. A. Cowie, 1990, Determination of total strain from faulting using slip measurements: Nature, **346**, 837-839, doi.org/10.1038/346837a0.

Singhroha, S., S. Chand, and S. Bünz, 2019, Constraints on gas hydrate distribution and morphology in Vestnesa Ridge, Western Svalbard Margin, using multicomponent ocean-bottom seismic data: Journal of Geophysical Research: Solid Earth, **124**, 4343–4364, doi.org/10.1029/2018JB016574.

Singhroha, S., S. Bünz, A. Plaza-Faverola, and S. Chand, 2020, Detection of gas hydrates in faults using azimuthal seismic velocity analysis, Vestnesa Ridge, W-Svalbard Margin: Journal of Geophysical Research: Solid Earth, **125**, e2019JB017949, doi.org/10.1029/2019JB017949.

Smart, K. J., D. A. Ferrill, and A. P. Morris, 2023, Geomechanical insights on the importance of mechanical stratigraphy to hydraulic fracture containment: American Association of Petroleum Geologists Bulletin, **107**, 1811–1835, doi.org/10.1306/07172321145.

Sultan, N., A. Plaza-Faverola, S. Vadakkepuliyambatta, S. Bünz, and J. Knies, 2020, Impact of tides and sea-level on deep-sea Arctic methane emissions: Nature Communications, **11**, 5087, doi.org/10.1038/s41467-020-18899-3.

Sztybor, K., and T. L. Rasmussen, 2017, Diagenetic disturbances of marine sedimentary records from methane-influenced environments in the Fram Strait as indications of variation in seep intensity during the last 35 000 years: Boreas, **46**, 212–228, doi.org/10.1111/bor.12202.

Vanneste, M., S. Guidard, and J. Mienert, 2005, Bottom-simulating reflections and geothermal gradients across the western Svalbard margin: Terra Nova, **17**, 510–516, doi.org/10.1111/j.1365-3121.2005.00643.x.

Vogt, P. R., K. Crane, E. Sundvor, M. D. Max, and S. L. Pfirman, 1994, Methane-generated(?) pockmarks on young, thickly sedimented oceanic crust in the Arctic: Vestnesa Ridge, Fram Strait: Geology, **22**, 255–258, doi.org/10.1130/0091-7613(1994)022<0255:MGPOYT>2.3.CO;2.

Waage, M., P. Serov, K. Andreassen, K. A. Waghorn, and S. Bünz, 2020, Geological controls of giant crater development on the Arctic seafloor: Scientific Reports, **10**, 8450, doi.org/10.1038/s41598-020-65018-9.

Wang, S., X. Si, Z. Cai, and Y. Cui, 2022, Structural augmentation in seismic data for fault prediction: Applied Sciences, **12**, 9796, doi.org/10.3390/app12199796.

Wood, W. T., P. E. Hart, D. R. Hutchinson, N. Dutta, F. Snyder, R. B. Coffin, and J. F. Gettrust, 2008, Gas and gas hydrate distribution around seafloor seeps in Mississippi Canyon, Northern Gulf of Mexico, using multi-resolution seismic imagery: Marine and Petroleum Geology, **25**, 952–959, doi.org/10.1016/j.marpetgeo.2008.01.015.

Wu, X., L. Liang, Y. Shi, and S. Fomel, 2019, FaultSeg3D: Using synthetic data sets to train an end-to-end convolutional neural network for 3D seismic fault segmentation, Geophysics, **84**, IM35–IM45, doi.org/10.1190/geo2018-0646.1.

Zhang, B. and Y. Lou, 2020, Automatic seismic fault surfaces construction using seismic discontinuity attribute, SEG Technical Program Expanded Abstracts, SEG, 1101-1105, doi.org/10.1190/segam2020-3427011.1.

Zhang, G., X. Wang, L. Li, L. Sun, Y. Guo, Y. Lu, W. Li, Z. Wang, J. Qian, T. Yang, and W. Wang, 2022, Gas hydrate accumulation related to pockmarks and faults in the Zhongjiannan Basin, South China Sea: Frontiers in Earth Science, **10**, 902469, doi.org/10.3389/feart.2022.902469.

LIST OF FIGURES

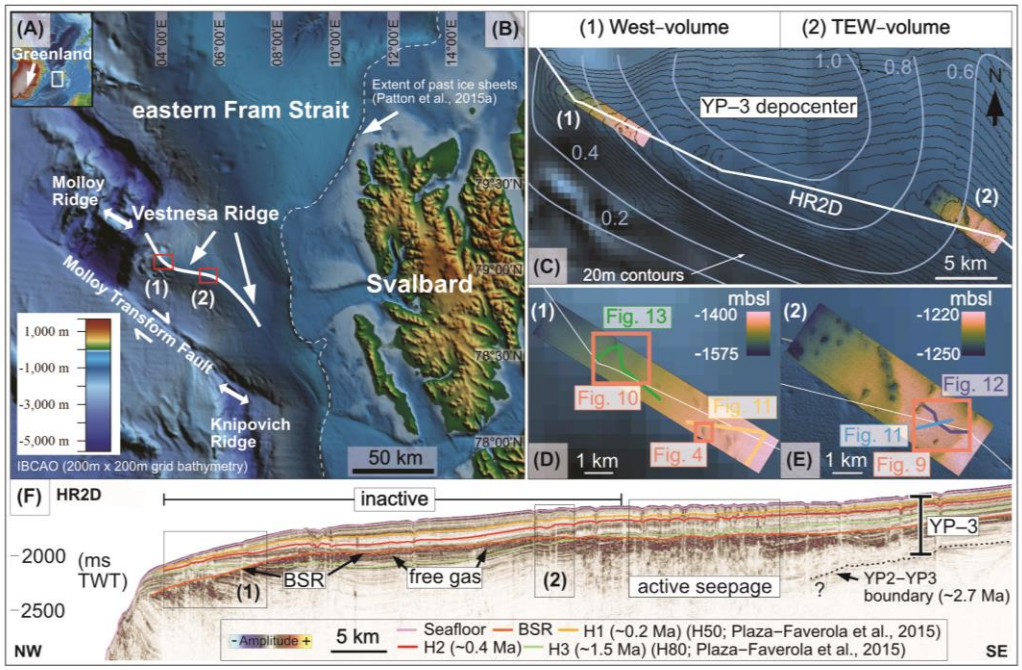


**Figure 1**. **(A)** Overview of the study area in the eastern Fram Strait. **(B)** Location of the areas along the Vestnesa Ridge investigated with 3D seismic data (red boxes). HR2D transect (white line) used in Plaza–Faverola et al., 2015, 2017. **(C)** Ridge bathymetry contours (black lines) and isopach contours (blue lines) of depth (seconds TWT) to the base of the Yermak Plateau stratigraphic marker (YP–3; adapted from Eiken and Hinz, 1993). **(D)** and **(E)** 3D seismic bathymetry (10 m x 10 m). **(F)** The HR2D seismic line providing a regional stratigraphic framework above the gas hydrate stability zone (i.e., above the bottom–simulating reflection (BSR) (modified after Plaza–Faverola et al., 2017).

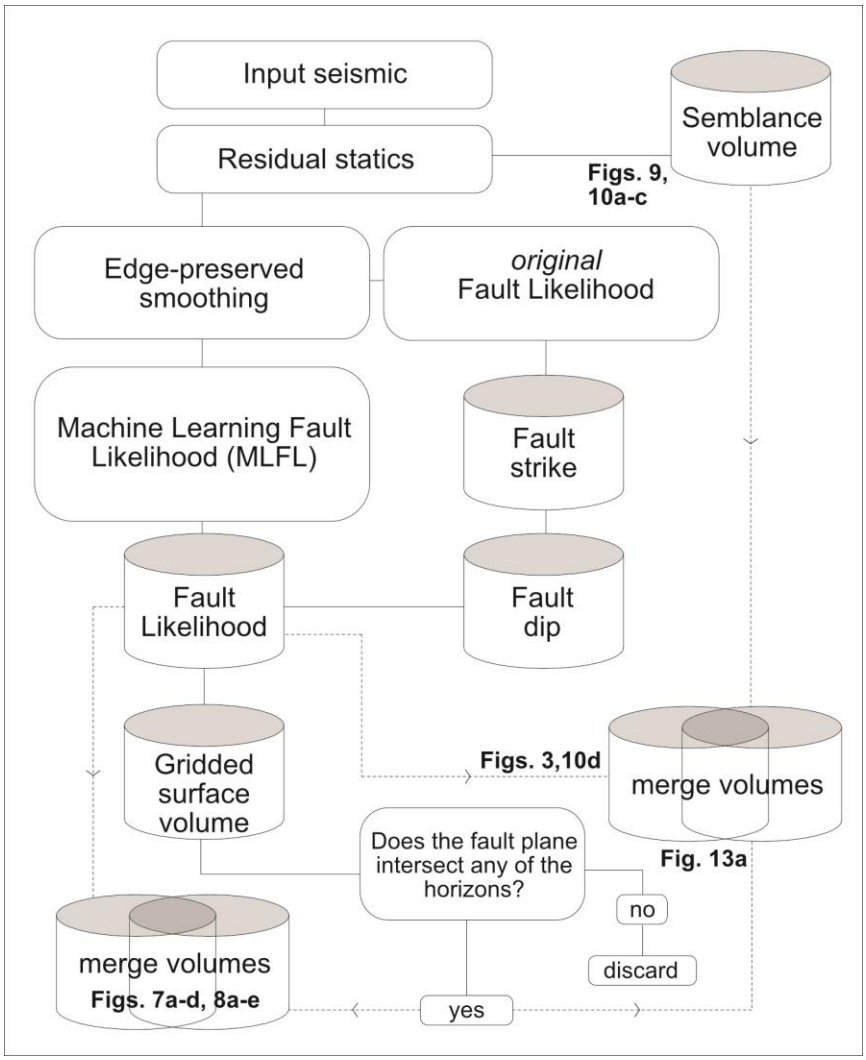


**Figure 2**. Seismic processing and attribute workflow. The original input seismic volume is preconditioned with residual statics and edge–preserved smoothing. After the preconditioning steps, the volume is input into the Machine Learning (ML) 3D U–Net to create a Machine Learning Fault Likelihood (MLFL) volume output. The fault dip and fault strike components from the original fault likelihood are used in the MLFL attribute calculation to create a gridded surface volume. Selected gridded surfaces are extracted as fault planes and merged with other volume attributes.

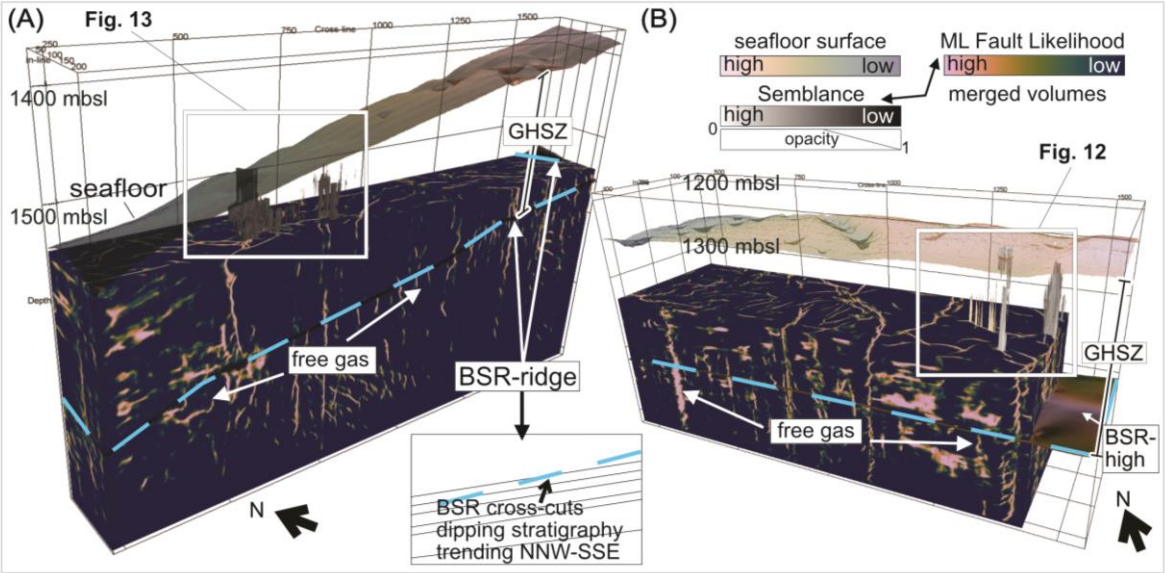


**Figure 3**. Subset of the Machine Learning Fault Likelihood (MLFL) volume merged with the semblance volume below the seafloor. The seismic attribute volumes are calculated from the original **(A)** West–volume, and **(B)** TEW–volume. The dashed blue line represents the bottom–simulating reflection (BSR) and where the BSR cross–cuts above the seismic stratigraphy. The gas hydrate stability zone (GHSZ) lies above the BSR and free gas is below.

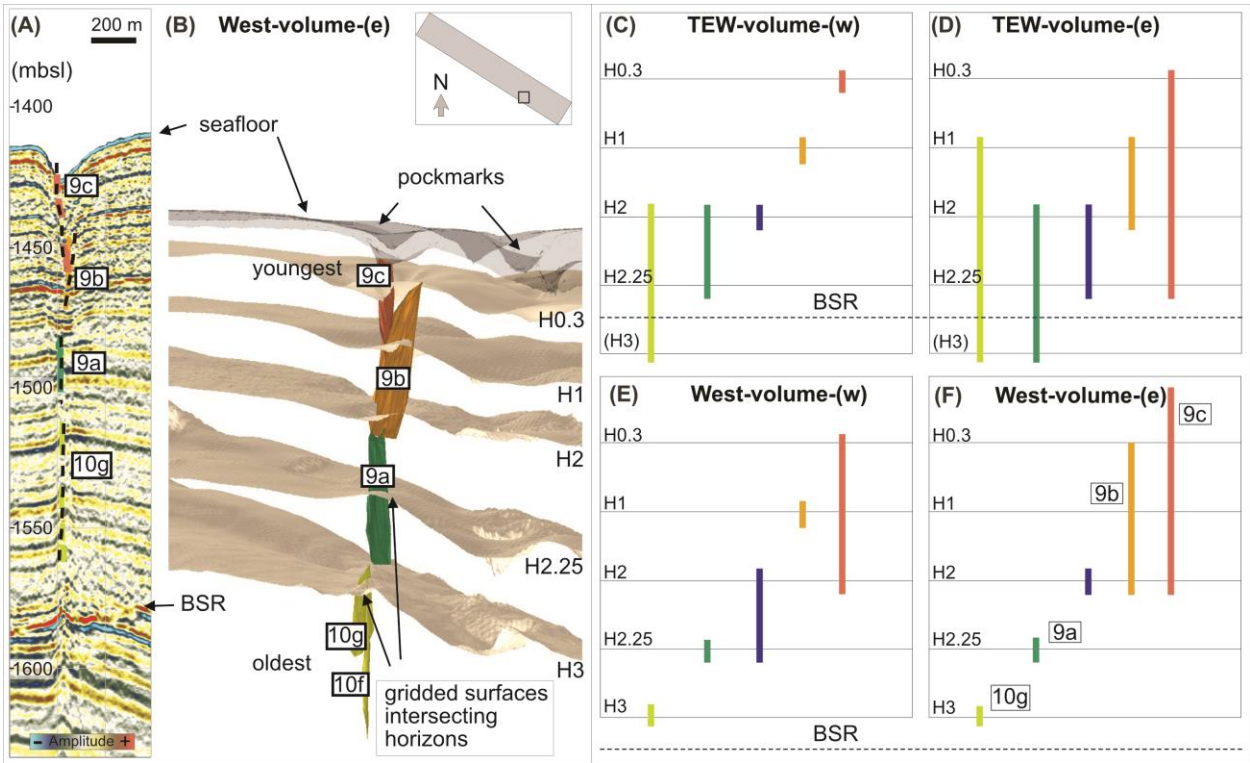


**Figure 4**. An example of fault plane extractions from the West–volume showing the profile irregularities of a fault **(A)** in 2D view with intersecting seismic section and **(B)** 3D view with surface horizons. The fault planes are color–coded according to assigned zones (oldest to youngest burial: yellow, green, orange and pink respectively). The fault planes are extracted because they intersect the horizons used in the interpretation (i.e., H0.3, H1, H2, H2.25 and H3). Note horizon H3 is used only in the West–volume because this horizon dips beneath the bottom–simulating reflection (BSR) in the TEW–volume. The age zones **(C)** to **(F)** show how many horizons are intersected by the fault planes.

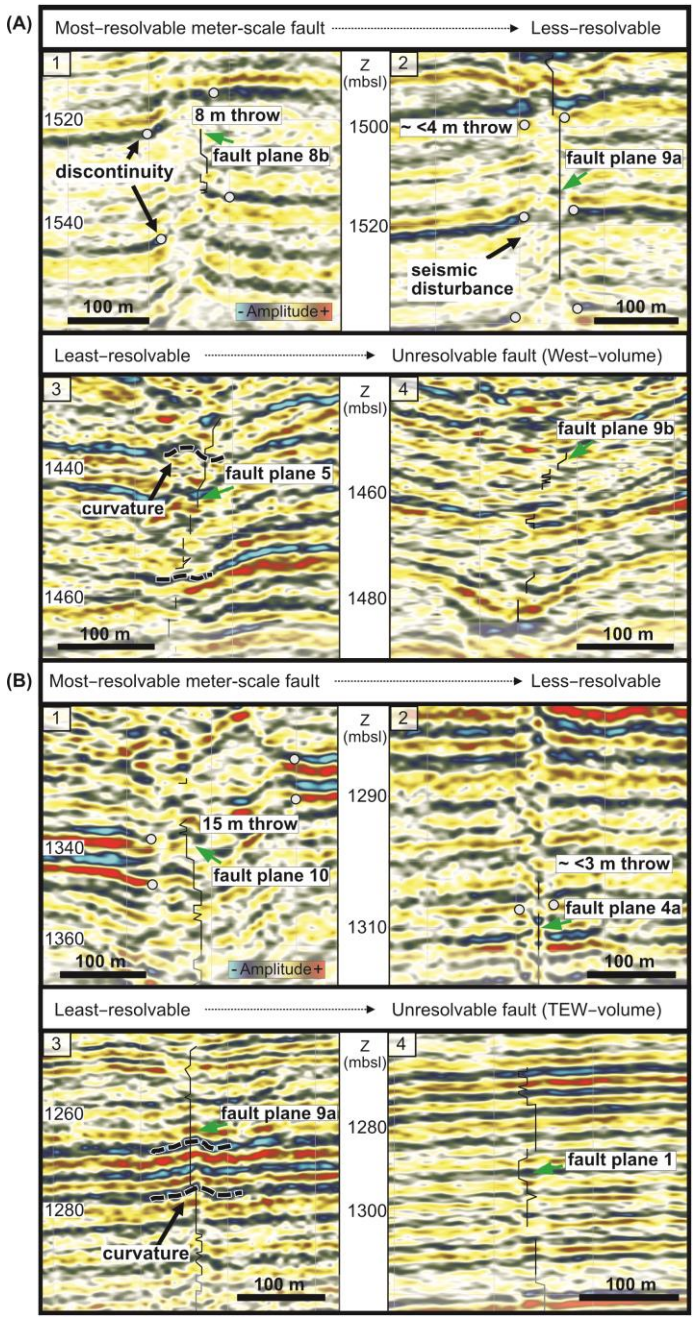


**Figure 5**. **(A)** Data examples in the West–volume, and **(B)** TEW–volume, show fault planes that are classified as **(1)** faults i.e., "most–resolvable" or **(2)** having throws at or slightly below the resolution of the data set i.e., "less–resolvable". **(3)** Fault planes are detected by subtle curvature and showing no throw "least–resolvable". **(4)** Fault planes are classed as "unresolvable" or "ambiguous" when they become difficult to see by eye in the seismic section.

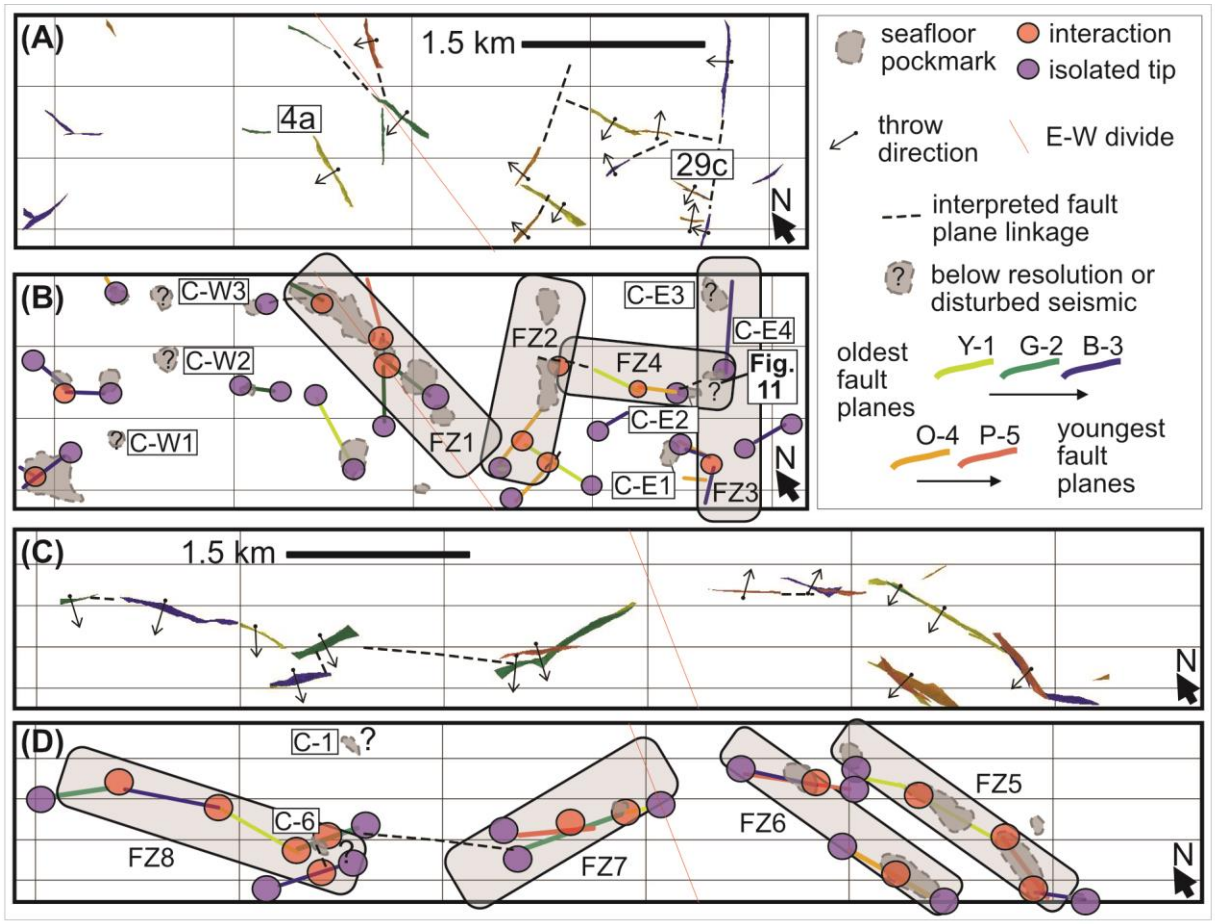


**Figure 6**. Map view of the extracted fault planes in the TEW–volume **(A)** and West–volume **(C)** with approximate throw (extension) direction marked by the arrows perpendicular to the faults. The fault planes are color–coded according to age zones as in Figure 4. The divide between the east and the west of each survey is marked by thin arbitrary red lines. Fault zones and chimneys are outlined respectively, and points of interaction and isolated fault plane tips interpreted **(B)** and **(D)**. Structures labeled with queries are not associated with extracted fault planes (C–W1, C–W2, C–W3, C–E3) or are within zones of disturbed seismic or at the edge of the survey (C–E4 (**B)** and C–1 and C–6 **(D)**).

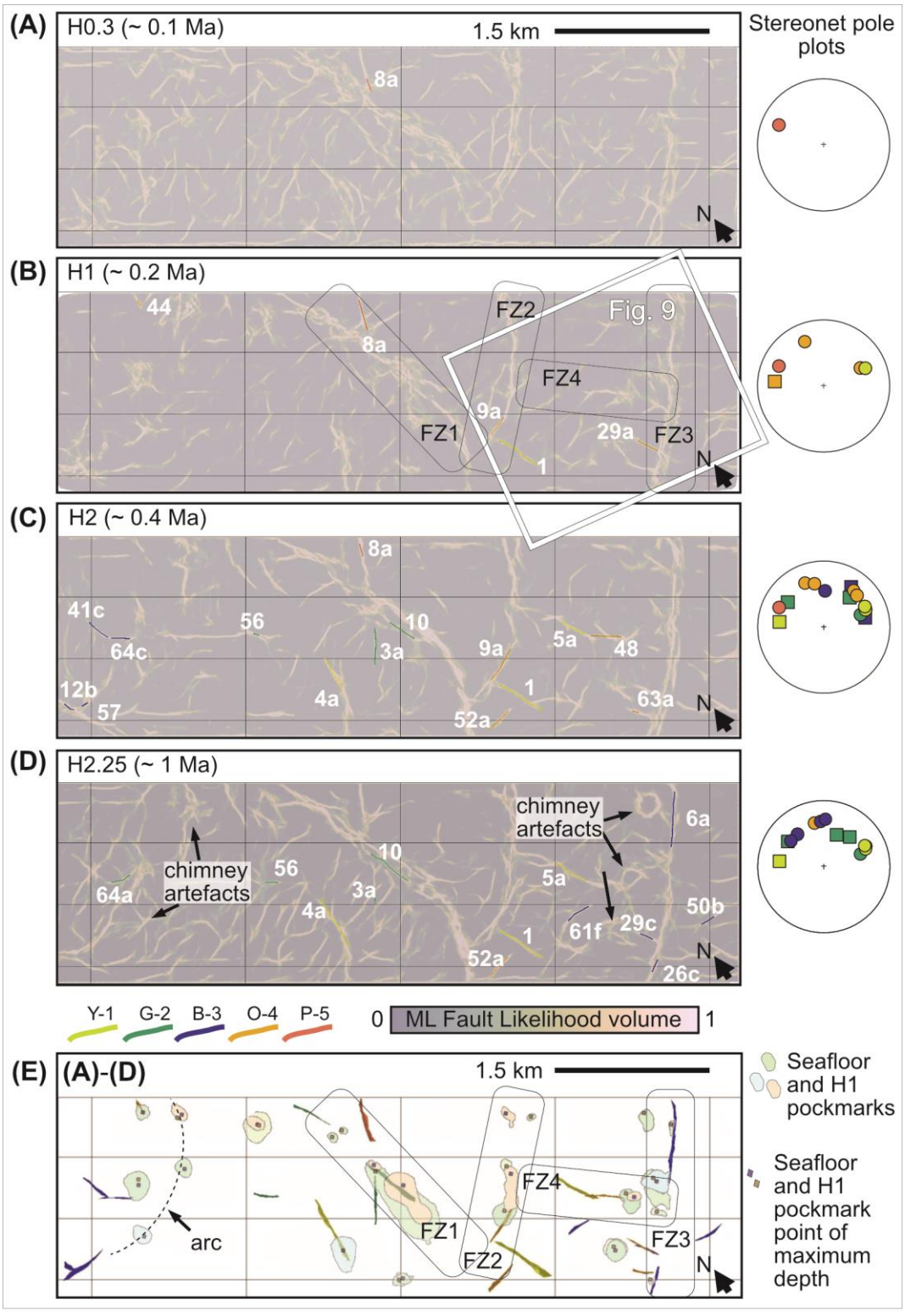
(A)
H0.3 (~ 0.1 Ma)
1.5 km
8a
N
Stereonet pole plots
(B)
H1 (~ 0.2 Ma)
44
8a
FZ2
Fig. 9
FZ4
9a
FZ1
29a
FZ3
1
N
(C)
H2 (~ 0.4 Ma)
8a
41c
56
10
64c
3a
9a
5a
48
12b
4a
1
63a
57
52a
N
(D)
H2.25 (~ 1 Ma)
chimney artefacts
6a
chimney artefacts
10
56
5a
64a
3a
50b
4a
61f
29c
1
52a
N
26c
Y-1
G-2
B-3
O-4
P-5
0
ML Fault Likelihood volume
1
(E)
(A)-(D)
1.5 km
Seafloor and H1 pockmarks
FZ4
arc
FZ1
FZ3
FZ2
N
Seafloor and H1 pockmark point of maximum depth

**Figure 7**. **(A)** – **(D)** TEW–volume, Machine Learning Fault Likelihood (MLFL) volume horizon surfaces H0.3 to H2.25 (~0.1–1 Ma). Fault zones (FZ1–4) are indicated. Intersecting (color–coded) fault planes to horizons are displayed at each respective horizon, blended with the transparent MLFL horizons. The stereonet pole plots represent faults (with throw; circles) and fault planes (no throw; squares). **(E)** Extracted pockmarks from two (10 m x 10 m) surfaces (seafloor and H1) using a rule–based GIS methodology (Patton et al., 2015b) are combined with fault plane extractions. The chimney artefacts and pockmarks in the west of the volume (C–W1, C–W2 and C–W3; Figure 6b), are arranged in an arc following the bathymetric contours.

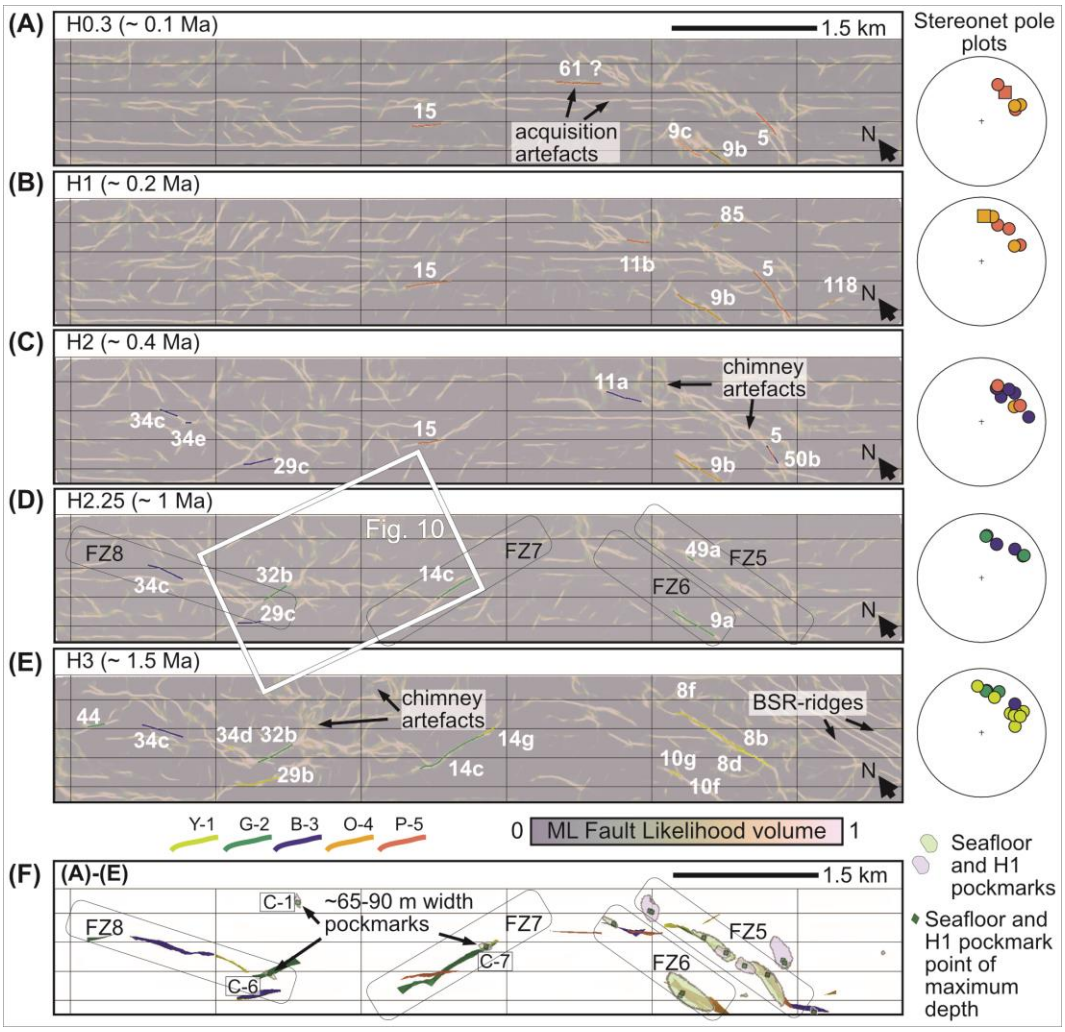


**Figure 8**. **(A)** – **(E)** West–volume, Machine Learning Fault Likelihood (MLFL) volume horizon surfaces H0.3 to H3 (~0.1–1.5 Ma). Note sail line artefacts **(A)** and "BSR–ridges" **(E)**; (also see Figures 3a and 11c, d). Intersecting (color–coded) fault planes to horizons are displayed at each respective horizon blended with the transparent MLFL horizons. The stereonet pole plots represent faults (with throw; circles) and fault planes (no throw; squares). **(F)** Extracted pockmarks from two (10 x 10 m) surfaces (seafloor and H1) using a rule–based GIS methodology (Patton et al., 2015b) are combined with fault plane extractions and pockmarks C–1, C–6 (Figure 6) and C–7 are labeled.

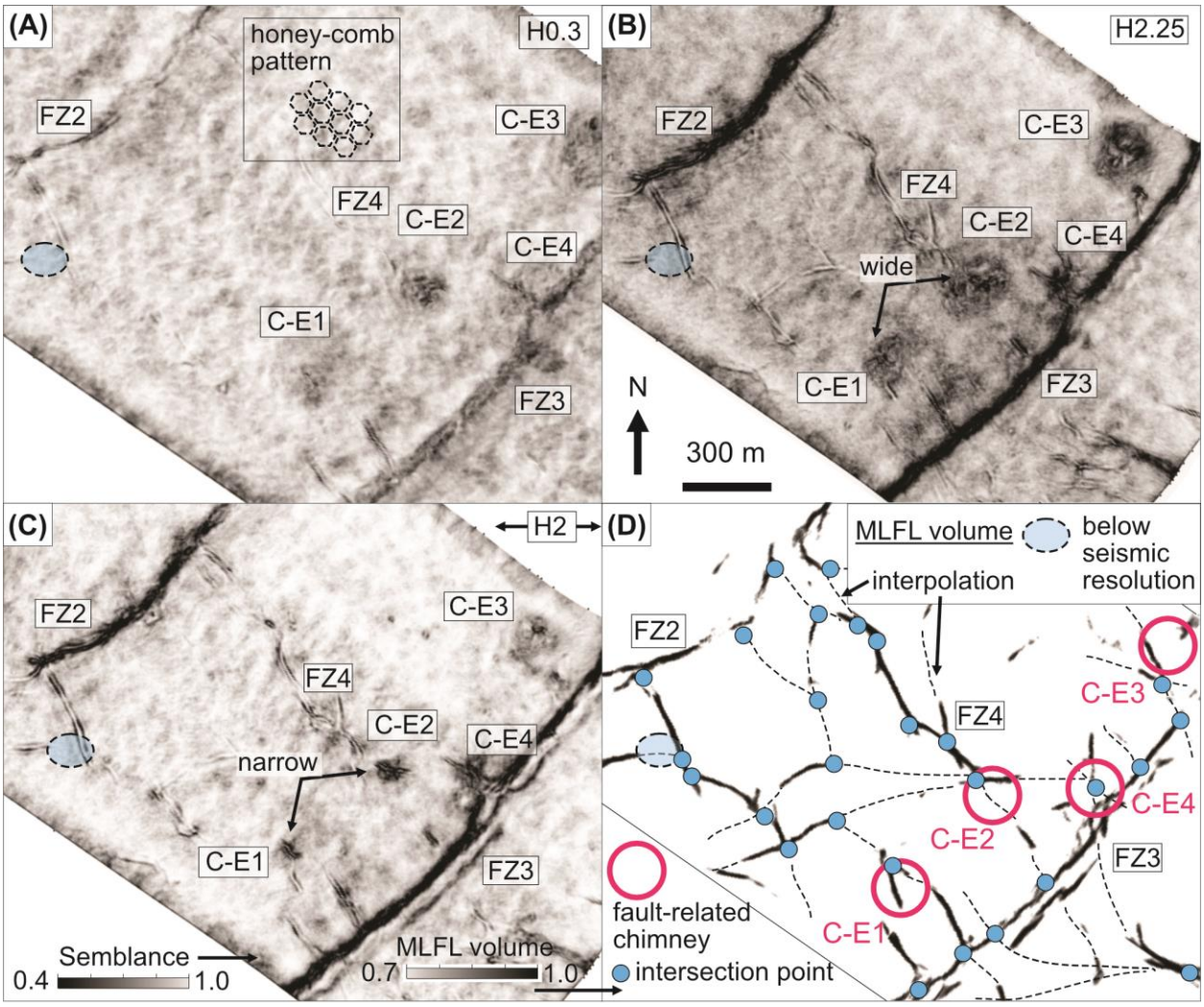


**Figure 9**. **(A)** TEW–volume, coherency at horizon H0.3 within the distributed gas leakage zone. Small–scale (~20–50 m) depressions inform a "honeycomb" pattern. **(B)** Coherency at horizon H2.25. Fault zone FZ4 is imaged well at horizon H2.25 and the box fault pattern is partially imaged. Chimneys C–E1, C–E2 and C–E3 are wider at **(B)** and narrower at Coherency horizon H2 **(C)**. **(D)** Machine Learning Fault Likelihood (MLFL) at horizon H2. Example of interacting planar features below the resolution of the data set (dashed blue filled oval) and fault related chimney C–E4 (pink circle) at the intersection point (blue filled circle) between FZ3 and FZ4 (see also Figure 11a). Other fault related chimneys and intersection points

between planar features are interpreted. The partially imaged box fault pattern is interpolated using the planar features imaged in the MLFL at horizon H2.

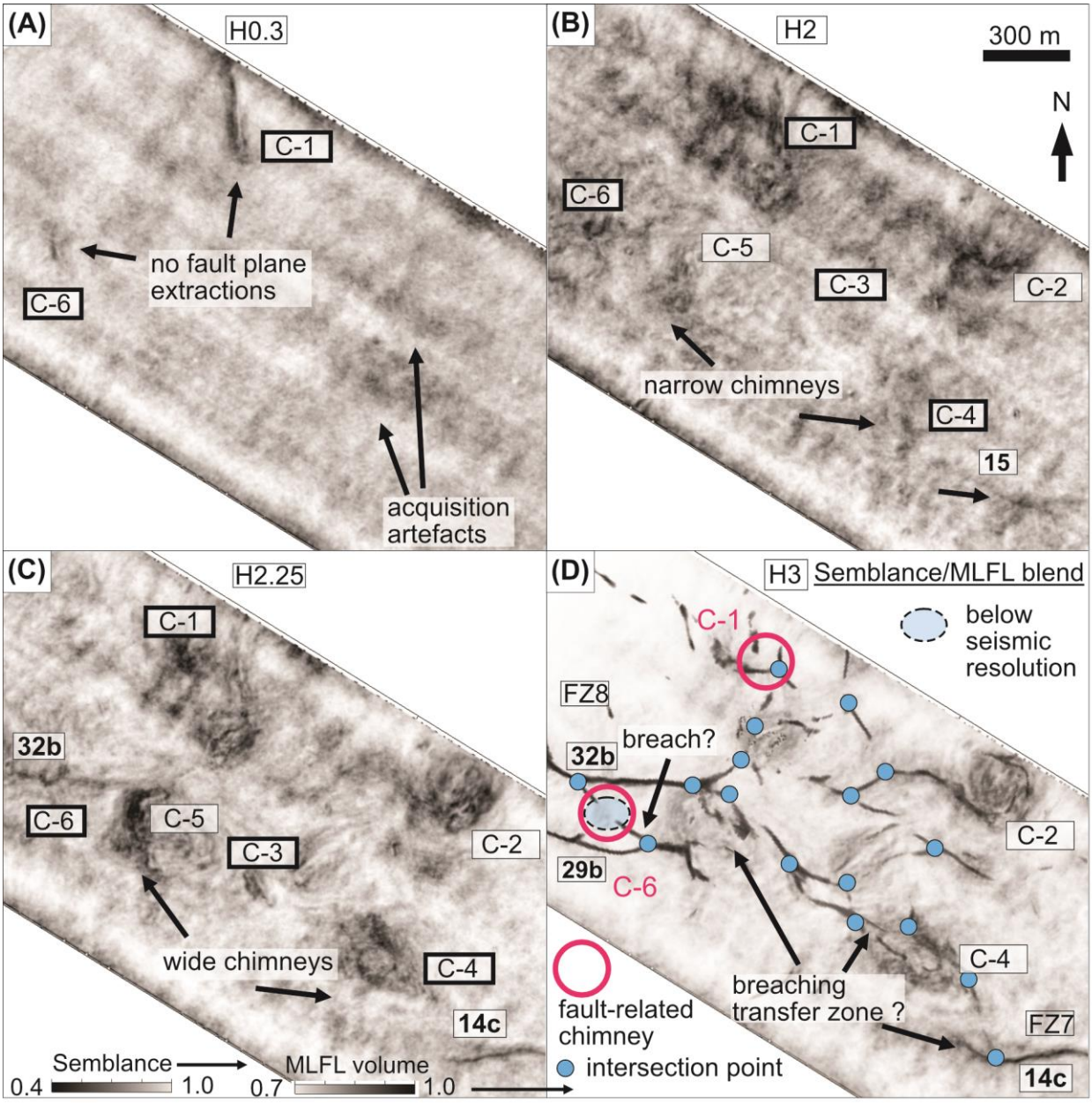


**Figure 10**. **(A)** West–volume, coherency at horizon H0.3 within the distributed gas leakage zone reveals artefacts (see also Figure 8a). Chimneys (displayed deeper in the volume) are absent in the shallowest horizon H0.3 except for the elongated depressions (C–1 and C–6). **(B)** Coherency at horizon H2. Chimneys C–4 and C–5 are less defined. Isolated fault planes *15* and *14c* exhibit a change in strike between horizons. **(C)** Coherency horizon at H2.25. Of the six chimneys (C–1 to C–6), those with bold outlined boxes are further illustrated (Figure 13). **(D)**

Attribute volume blend of Machine Learning Fault Likelihood (MLFL) and semblance at horizon H3 indicating fault–related chimneys (pink circles) and example of planar features at or below the limit of resolution (dashed blue filled oval). Breach is interpreted between fault planes *32b* and *29b* (see also Figure 13a) and transfer zone between fault planes *32b* and *14c*. Intersection points between planar features are interpreted (blue filled circles).

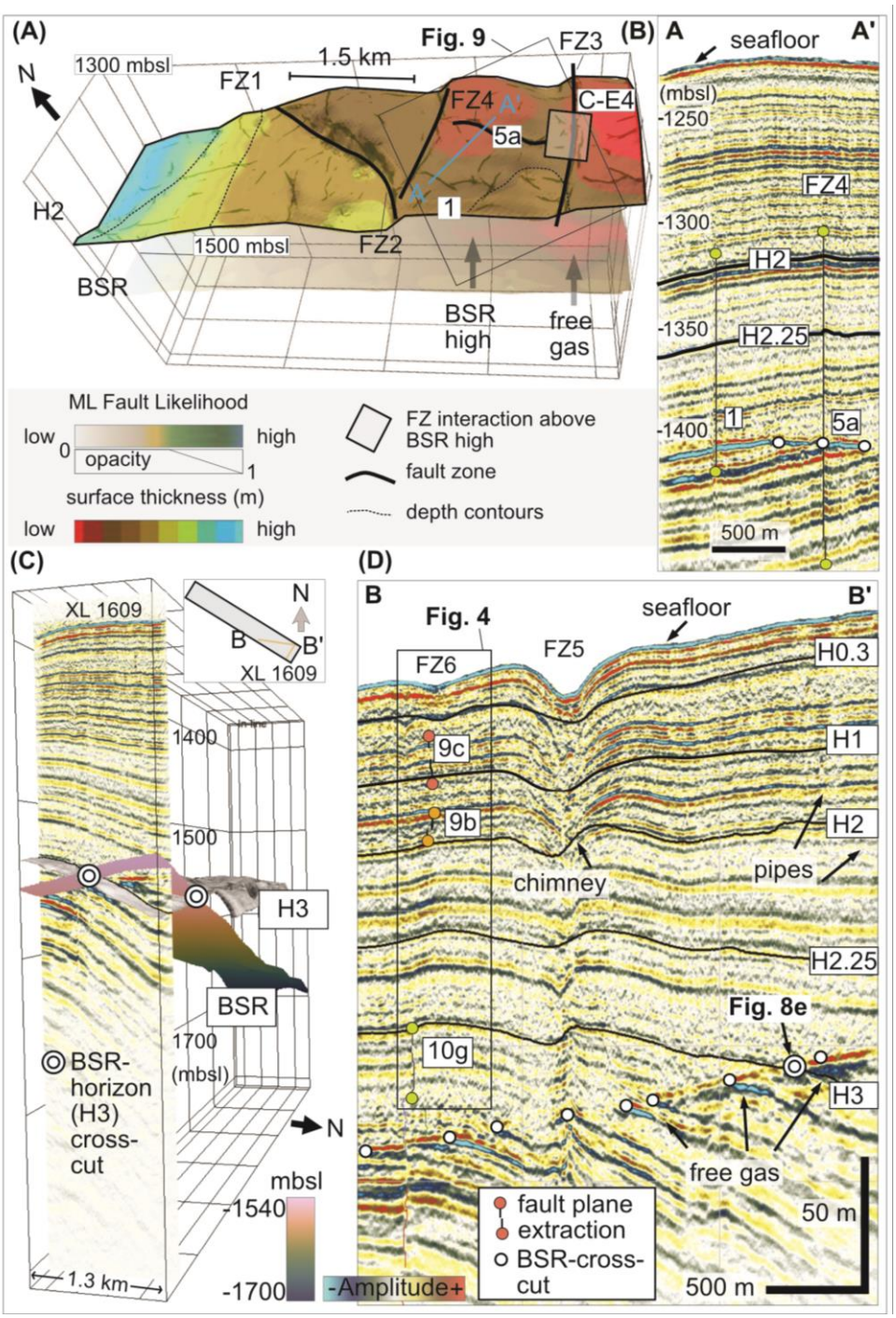


**Figure 11**. **(A)** TEW–volume horizon isopach between H2 and the seafloor and between the BSR reflection and the seafloor (transparent). The "BSR–high" lies directly beneath the fault zone (FZ) interaction (i.e., T-junction between FZ3 and FZ4), where the chimney at this junction

distorts the seismic imaging. **(B)** Section A–A' intersects fault planes *1* and *5a*: within fault zone FZ4. "BSR–crosscuts" are highlighted (white filled circles) and the ends of extracted fault planes (*1* and *5a*) are marked (yellow filled circles). **(C)** Cross–line (XL) 1609, displays the cross–over points (bullseyes) where H3 cross–cuts the BSR (see artefacts in Figure 8e) and deepens towards the west. **(D)** Section B–B' displays examples of phase–reversed high amplitude anomalies (see Figure 13b) terminating at the BSR and pipes above. The colored (yellow, orange, and pink) filled circles mark the ends of the extracted fault planes (thin lines) intersecting the seismic. Note the absence of high amplitudes at the BSR within the region of the chimney.

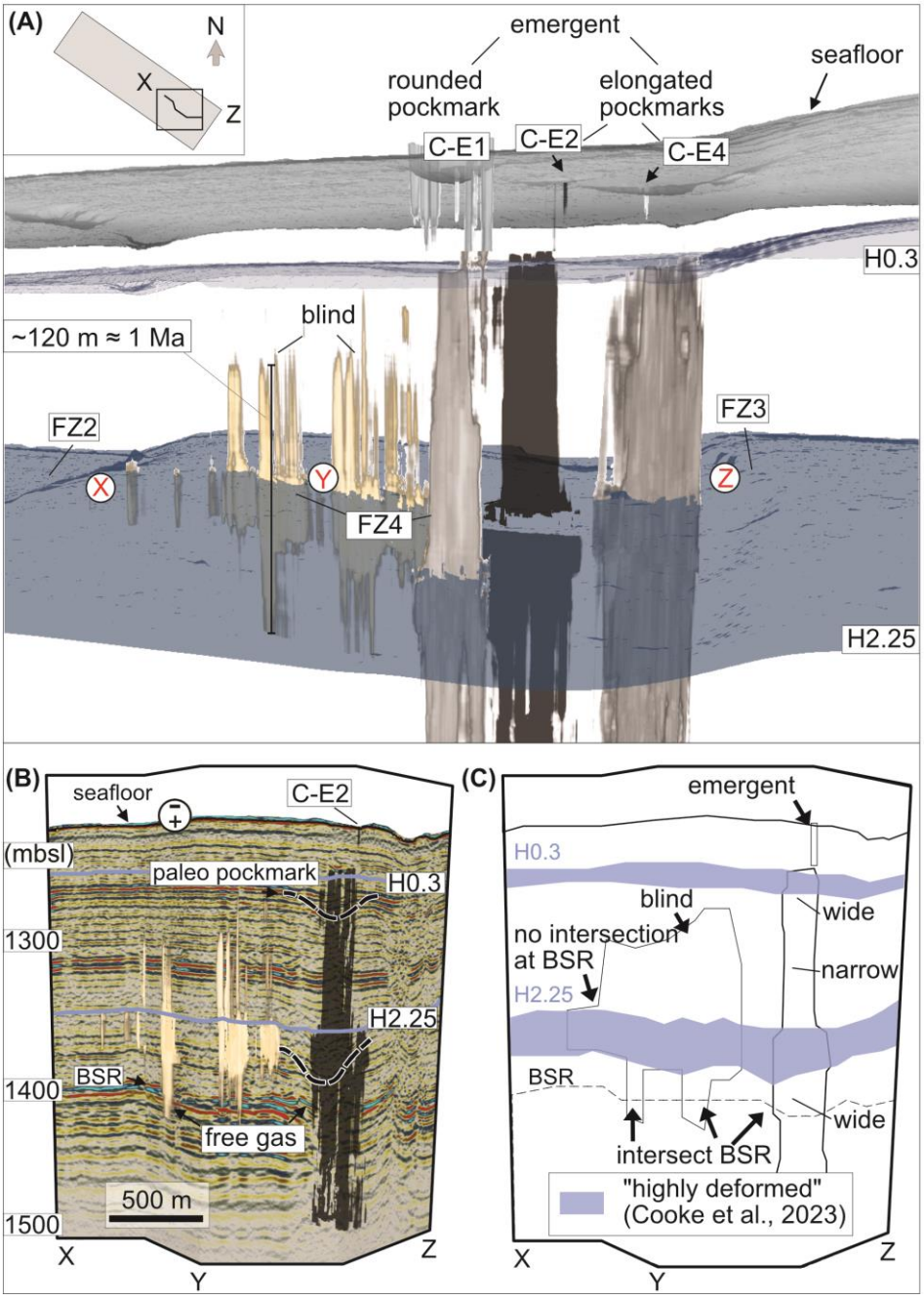


**Figure 12**. **(A)** TEW–volume, 3D view of the coherency chimneys (C–E1, C–E2, C–E4) within the distributed gas leakage zone. The chimneys are color–defined according to whether they are "blind" (light brown) or "emergent" (black and gray). **(B)** Section (X–Y–Z) displays the original seismic, blended with the chimneys and two buried "paleo pockmarks" (dashed black

lines). Note the thickening of chimney C–E2 between the BSR and horizon H2.25 and again at horizon H0.3. The blue polygons define “highly deformed” units (after Cooke et al., 2023) and coincide with chimney widening **(C)**.

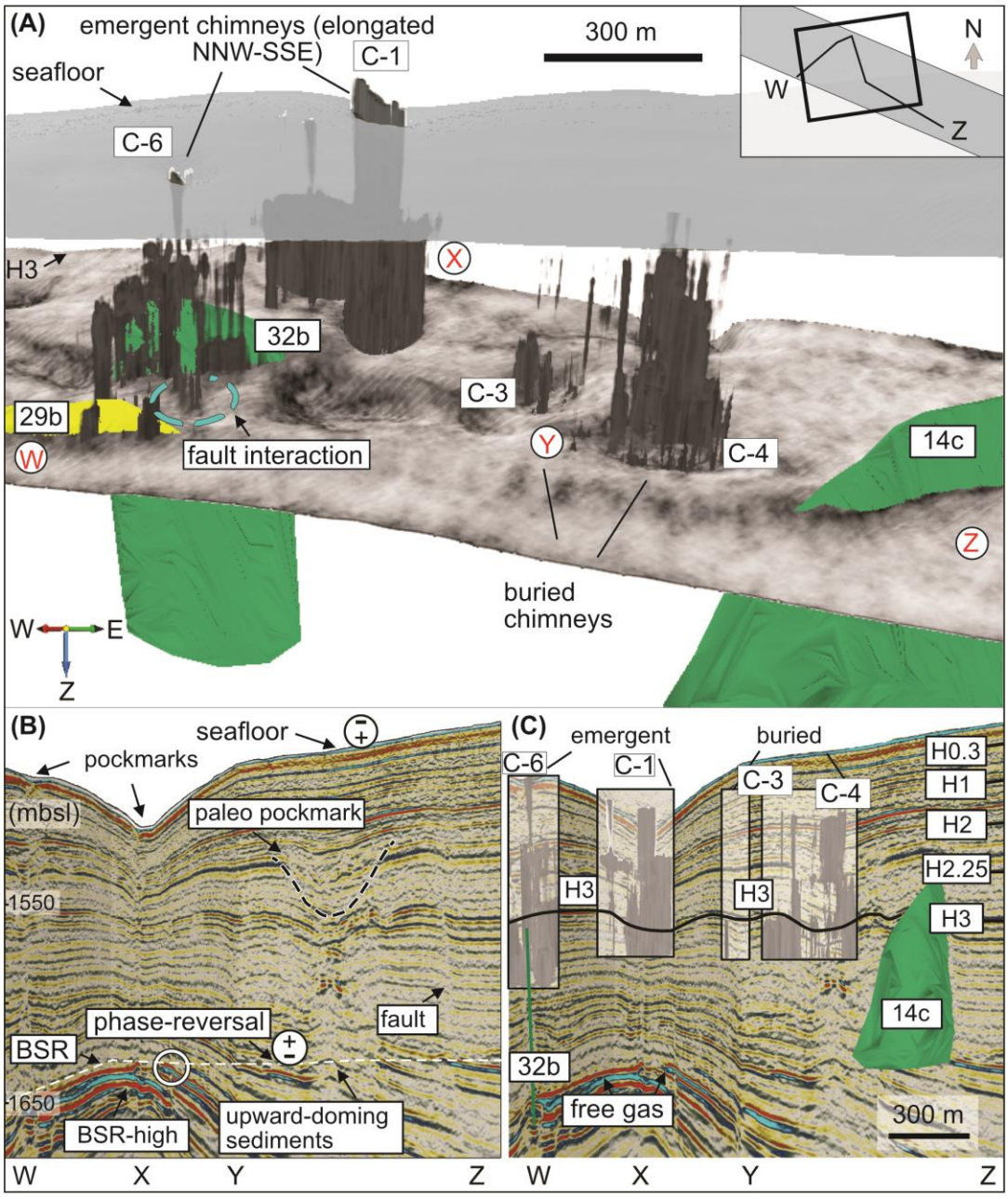


**Figure 13**. **(A)** West–volume, 3D view of the coherency chimneys (C–1, C–3, C–4, C–6) within the distributed gas leakage zone and fault planes (*29b*, *32b* and *14c*) intersect coherency horizon H3. The chimneys are grouped into types: 1) "emergent" chimneys (C–1 and C–6); 2) "buried" and "blind" (at point "Y"). The interaction between fault planes *29b* and *32b* (open dashed blue circle) is indicated. **(B)** – **(C)** Section (W–X–Y–Z) intersects seafloor pockmarks

and chimneys at C–1 and C–6 and paleo pockmarks at “Y”. A “BSR–high” occurs beneath C–1 at “X” and high amplitudes below the BSR are phase–reversed. Note upward doming seismic reflections located directly above the BSR (between points Y and Z).

## LIST OF TABLES

# APPENDIX A

**Table A–1**. Definition of structural and seismic interpretation terms

| **Structural term** | **Definition and key references** |
|---|---|
| Box–faults | A network of faults developed between two overstepping normal faults, described in the East African Rift by Griffiths (1980) |
| Deformation band | mm-scale tabular zones of localized but non-discrete strain, typically involving grain reorganization, cataclasis and/or dissolution or precipitation (e.g., Peacock et al., 2016) |
| Distributed gas leakage zone | We introduce the term in this study to refer to where gas is leaking but does not appear to be strongly channelized by faults interpreted in the seismic data. The definition is based on an observation rather than interpretation. |
| Fault | Price (1966) defines a fault as "a plane of fracture which exhibits obvious signs of differential movement of the rock mass on either side of the plane. Faults are therefore planes of shear failure". Faults tend to be zones of deformation, consisting of multiple slip surfaces, subsidiary fractures and perhaps deformation bands (e.g., Fossen, 2010). In the context of seismic, a fault is a planar feature event with a visible offset between reflection events on either side. |
| Fault dip and strike | Any planar feature can be described by dip and strike to determine its orientation. Fault strike is the azimuth across the plane, and fault dip is the angle of inclination measured downward from the horizontal (e.g., Fossen, 2010). |
| Fault extraction | As defined in this study, an automated process by which seismic faults are extracted from a "fault likelihood" volume. The extracted faults are represented as grids, which are called fault "gridded surfaces". The gridded surfaces can be transformed into "fault planes", the common name (format) for faults in seismic data. |
| Fault likelihood | A volume that gives at every seismic sample position on a scale of 0 to 1, the likeliness of this position being located at a fault. The original fault likelihood attribute by Hale (2013), outputs three components: fault likelihood, dip of fault likelihood, and strike (azimuth) of fault likelihood. |
| Fault plane | In a structural interpretation context, the fault plane is a surface along which there has been displacement. As defined in the study, a fault plane in seismic interpretation software is a plane that is created/visualized on–the–fly and is generated by fault sticks (e.g., Zhang and Lou, 2020). In this study faults and planar features are interpreted from fault planes. |

| | |
|---|---|
| Fault stick | A set of vertical or horizontal lines representing a fault plane (e.g., Zhang and Lou, 2020). |
| Fault zone | A system of related fault segments that interact and link and are restricted to a relatively narrow band or volume (e.g., Peacock et al., 2016). |
| Fault network | A system of linked and interacting faults, more diffuse than a fault zone (Peacock et al., 2000). |
| Fracture | Fractures include dikes, faults, joints and veins. Fracture appears to be synonymous with discontinuity (Priest and Hudson, 1976, 1981 from Peacock et al., 2000). A fracture in a seismic context is a planar event without a visible offset between reflection events on either side. |
| Gridded surface | As defined in this study, a gridded surface refers to a grid of points belonging to the same fault. Also defined in the literature as "fault surface patch" (e.g., Zhang and Lou, 2020) |
| Machine Learning Fault Likelihood (MLFL) | As defined in this study, a machine learning model predicts fault likelihood (scale 0 to 1). It does not predict fault dip and fault strike (azimuth). To apply a thinning algorithm, or to automatically extract faults from MLFL, these missing components need to be computed first. This is done by applying the original fault likelihood algorithm on a "flipped" MLFL (1 minus MLFL). |
| Planar feature | As defined in this study, a structure in seismic data observed in the MLFL volume as a discontinuity which does not have a throw because it is probably below the resolution of the data set. |
| Transfer zone | A transfer zone is formed between two stepping faults with interacting tips (e.g., Peacock et al., 2000). The transfer zone may contain several faults and smaller structures, which cross–cut and breach the transfer zone (e.g., Morley et al., 1990) |

**Table A–2**. Interpretation summary of the TEW–volume

| | **TEW–volume–(w)** | **Central** | **TEW–volume–(e)** |
|---|---|---|---|
| Fault zones (FZ) | – | FZ1 | FZ2 and FZ3 |
| Structural characteristics | -No throw is observed, except for fault plane *4a* (throw is at the limit of the resolution ~ <3 m).<br>-Planar features are interpreted where no throw is observed *(e.g.,41c, 64c, 12b, 57).*<br>-Many of the fault planes are ambiguous (i.e., unresolved) | -FZ1 strikes ~N–S.<br>-The largest fault throw is ~15 m at fault plane *10,* while all other faults are at or below the limit of resolution (~ <3 m). | -FZ2 and FZ3 strike NE–SW, and FZ4 is perpendicular to and bound by FZ2 and FZ3.<br>-The interpreted box–faults within the distributed gas leakage zone have ~N–S and ~NNW–SSE strike orientations.<br>-Fault and planar feature networks within the distributed gas leakage zone appear unresolved or at the limit of the resolution (~ <3m). |
| Pockmark presence and fault–related/fault independent fluid flow indications | -Possible chimneys not related to faults, observed to follow the depth contours of the seafloor.<br>-Pockmarks located above fault planes (e.g., 4a, 48) (i.e., at horizons H1, H2.25) indicate that the structures act as conduits for long term fluid flow (Fig. 7e).<br>-Fault planes (e.g., *12b, 57, 64a* and *c, 41c* and *44)* intersect chimneys (Fig. 7b, c, d, e). | -Seafloor pockmarks are present where fault planes are interacting (e.g., *8a–3a,* and *10)* (Fig. 7b). | -Seafloor pockmarks are located at the tips of fault planes (e.g., *29c, 4a, 6a).*<br>-Seafloor pockmarks exist at a distance away from the tips of the fault planes (e.g., *29c)* (Fig. 7d, e). |
| Fault interaction (i.e., abutting, stepping, individual vertical linkage of fault planes, and transfer structures) | -Interacting fault plane examples (e.g., *12b*, *57*, *5a, 48 and 41c, 64c)* at horizon H2 (Fig. 7c).<br>-Some fault planes exhibit a change in strike, between horizons (e.g., *56* and *64a–64c),* between horizons H2.25 and H2 (Fig. 7c–d). | -Interacting fault plane examples (e.g., *10, 3a* and *8a)* at horizon H2 (Fig. 7c). | -Individual fault planes (e.g., *29a,* and *29c)* have the same strike at horizons H2.25 and H1 (Fig. 7b, d).<br>-Fault planes (e.g., *1, 5a, 52a, 48, 61f, 29c)* located between FZ2 and FZ3 are probably influenced by transfer structures. |

**Table A–3**. Interpretation summary of the West–volume

| | **West–volume–(w)** | **West–volume–(e)** |
|---|---|---|
| Fault zones (FZ) | FZ7 and 8 | FZ5 and 6 |
| Structural characteristics | -FZ7 strikes ~NW–SE and FZ8 strikes ~NE–SW.<br>-Fault throws are larger than in the TEW–volume. Fault planes in the West–volume–(w) (e.g., *14c, 14g)* have the largest throws (i.e., 6 and 7 m), while all others are at the limit of the resolution ~ <4 m.<br>-Fault zones FZ5–8 are separated into segments, some of which range in strike from 139–97° strike (e.g., *34c and 32b)* (Fig. 8a–f). | -FZ5 and 6 strike ~NNW–SSE.<br>-Fault throws are larger than in the TEW–volume. Fault planes (e.g., *8f, 8b, 8d)* have the largest throws, while all others are at the limit of the resolution ~ <4 m, or are ambiguous (e.g., *9b, 50b, 10f)*.<br>-Segments from FZ5 and FZ6 have comparable orientations (~NW–SE–WNW–ESE) to FZ1 in the TEW–volume and to FZ8 in the West–volume–(w) (e.g., fault plane *34c*). |
| Pockmark presence and fault–related fluid flow indications | -Fewer pockmarks exist in the West–volume–(w) compared to the TEW–volume–(w). They are more rounded at the intersection of fault plane*s (e.g., 14g* and *14c)*.<br>-Some buried chimneys, and buried pockmarks exist between FZ7 and FZ8 (Fig. 10).<br>-Emergent chimneys follow the largest fault–related seafloor pockmark orientation (i.e., ~NW–SE). | -Large (~200–500 m) fault–oriented pockmarks exist at the seafloor, oriented ~NW–SE to WNW–ESE.<br>-The most distinct (i.e., largest) fault planes are the oldest faults, oriented NNW–SSE to NW–SE (e.g., *11a, 10g, 10f, 8d, 8b, 8f, 5* and *50b)* (Fig. 8e). |
| Fault interaction (i.e., abutting, stepping, individual vertical linkage of fault planes, and transfer structures) | -The ENE–WSW fault plane segments between FZ7 and FZ8 (i.e., *32b, 29b, c)* (Fig. 8c–f), do not show pockmarks in alignment with the fault orientations at the seafloor. Rather, pockmarks adjacent to fault planes *(32b* and *29b)* are observed in a ~NW–SE orientation (Fig. 8f).<br>-An example of superposition of fault planes *14g, 14c* and *15* (Fig. 8 a–f). The oldest fault plane segment, 14g connects with a younger fault plane segment *14c* above which, fault plane *15* has rotated at a shallower horizon, from NE–SW to ~ E–W. | -The NW–SE oriented and WNW–ESE fault plane segments at FZ5 and FZ6 contain the largest seafloor pockmarks where segments have interacted (Fig. 8f).<br>-An example of fault interaction at FZ7 (Fig. 4) provides the evolution of a fault system. |

| |
|---|
| -A distributed gas leakage zone is interpreted between FZ7 and FZ8. |

**Table A–4**. Seafloor pockmarks and predicted fluid flow mechanisms for each seismic volume

| | **TEW–volume** | **West–volume** |
|---|---|---|
| Seafloor pockmark count and identification | **12 total** (C–W1, C–W2, C–W3, C–E1, C–E2, C–E4; Figure 6, 6 blue polygons unlabeled west of "C–W" pockmarks; Supplementary Figure S–7) | **8 total** (C–1 and C–6; Figure 6, 6 blue polygons labeled 1–6; Supplementary Figure S–8) |
| Surface area/pockmarks per unit area | 14.15 $km^2$ / **0.85** | 12.42 $km^2$ / **0.64** |
| Pockmarks per unit area related to fault planes only (or unknown source) | **0.49** (7 total: C–E1, 6 unlabeled; Supplementary Figure S–7) | **0.24** (3 total: C–1 and C–6; 1 labeled (i.e., 1); Supplementary Figure S–8) |
| Pockmarks per unit area related to BSR where fluid migration occurs | **0.35** (5 total: C–W1, C–W2, C–W3, C–E2, C–E4); Supplementary Figure S–7 | **0.40** (5 total: labeled 2–6; Supplementary Figure S–8) |

# APPENDIX B

**Table B–1**. Structural interpretation summary of the TEW–volume and West–volume

| **TEW–volume** | |
|---|---|
| Distributed gas leakage zone | Distributed gas leakage in the TEW–volume is interpreted between FZ2 and FZ3, an area that also shows paleo gas leakage, indicating later sealing of the structures.<br>There are blind or buried chimneys that do not emerge at the seafloor in both of the distributed gas leakage zones (Figures 12 and 13). There are relatively few pockmarks in these areas, and those that do exist are relatively smaller than pockmarks elsewhere in the study areas (Supplementary Figures S–7, S–8, and S–11). |
| Chimneys | Blind chimneys within the TEW–volume exhibit their maximum width at ~1 Ma, followed by a decrease in thickness continuing until ~0.4 Ma, and subsequently, a further reduction in thickness until ~0.2 Ma, where the emergent chimney widens a second time (Figure 12), which may imply a lithological control. |
| Fault interaction | The shallowest BSR burial aligns with the strike of FZ4, which cross–cuts FZ3 and continues in an E–W direction towards FZ2 (Figures 3b and 11a). The shallow depth to the BSR is most probably influenced by a transfer zone (see section "Transfer zones"). Seismic imaging in the zone of fault interaction (i.e., between fault planes *48* and *6a*; Figure 11a) is compromised by gas chimney "C–E4" (Figure 12; Supplementary Figure S–7), thereby affecting interpretation (Figures 6a–b). The arrangement of pockmarks labeled as "C–E1", "C–E2", "C–E3" (Figures 6b, and 9), aligned parallel to and situated approximately ~0.5 km away from the center of FZ3, may indicate gas migration could occur along or around breaching faults in the transfer zone.<br>Several types of fault interactions appear to occur in the TEW–volume, including relay ramps (i.e., a type of transfer zone) (e.g., Larsen 1988; Peacock and Sanderson 1991) and potential box–faults (e.g., Griffiths 1980), and these appear to influence fluid leakage. Fluid leakage is also known to be possible where faults interact (e.g., Gartrell et al., 2004; Ligtenberg, 2005; Michie and Braathen, 2023). Fault interactions like those in the TEW–volume are not observed in the West–volume. The lack of similarity between the two volumes is more likely attributed to geological differences rather than data quality.<br>Fault interaction appears to influence fluid flow in the |

| | |
|---|---|
| | TEW–volume–(e) area more than in the TEW–volume–(w), given the abundance of closely spaced fault zones imaged (FZ1–4) with highly varied orientations of the fault planes (Supplementary Figure S–4). As a result, more chimneys and pockmarks exist in the TEW–volume–(e). The interacting fault planes within fault zones probably contribute to fluid release facilitated by dilation (e.g., Gartrell, 2005). This means that fluid flow may not follow along the entire length of each fault but is channelized at points, where there may be sub–resolution structures such as fault steps or bends. For example, dilation is likely to have occurred where fault planes *3a*, *10* and *8a* intersect at a triple–point at FZ1 (Figure 7c, e). The transfer zone observed along the strike of FZ4 (Figures 6b, 7e, 9) is unique to the TEW–volume–(e). |
| Transfer zone | A possible example of a transfer zone occurs in the TEW–volume–(e) area, with <1–2 km between stepping fault zones FZ2 and FZ3. The two parallel fault zones are NE–SW striking, and connected by the breaching FZ4, which is nearly perpendicular to FZ2 and FZ3 (Figures 7, 9, 11a). |
| The gas hydrate–free gas interface (BSR) and influences on fluid flow | The irregular–shaped pockmarks and chimneys in the TEW–volume–(e) (e.g., C–E2 and C–E4) indicate that the BSR–high at FZ4 may have been influenced by the breached transfer zone. The migration of gas updip, from beneath the BSR in the TEW–volume–(w) area, also appears to be influential over the pattern of emergent chimneys and pockmarks (C –W1, C –W2 and C –W3), and are arranged in an arc following the bathymetric contours. Fault planes were not extracted and therefore no evidence of fault interaction was found within the chimneys in the TEW–volume–(w). The chimneys there are more rounded than those in the TEW–volume–(e) where pockmarks are irregularly shaped. |
| BSR depth | The BSR is situated above the lowermost interpreted horizon (H3) |
| **West–volume** | |
| Distributed gas leakage zone | There is an area of distributed paleo gas leakage in the West–volume between FZ7 and FZ8, indicated by a relatively high density of fault planes in the machine learning fault likelihood volume horizon slices and buried fluid flow features; of these, the buried fluid flow features are more convincing than the high density of fault planes (e.g., H3; Figure 8e).<br>Extractions of fault planes are lacking in the distributed gas leakage zone in the West–volume (Supplementary Figure S–3, i.e., "gridded surface absence"), despite the area showing a high likelihood of such features in the machine learning fault likelihood volume (Figure 8e). It is possible that the anomalies associated with sail line artefacts, prominent in the shallow horizons (i.e., H0.3 and H1), may obscure the imaging of the distributed gas leakage zone there. |

| | |
|---|---|
| Chimneys | The buried chimney ("Y") in the West–volume shows a paleo pockmark between horizons H3 and H2 corresponding to the period ~1.5–0.4 Ma (Figure 13). The chimney is narrow above the paleo pockmark and a pockmark absence is noted above this part of the chimney (i.e., it has become blind between the period ~0.4–0.2 Ma). |
| Fault interaction | Fault interactions like those in the TEW–volume are not observed in the West–volume. The lack of similarity between the two volumes is more likely attributed to geological differences rather than data quality.<br>The relatively small pockmark (90 m width x 125 m length) on the seafloor at FZ7 is positioned at the intersection between fault planes 14g and 14c (Figure 8e, f). |
| Gas hydrate–free gas interface (BSR) and influences on fluid flow | The association observed between the BSR–ridges (Figure 8) and the alignment of fault planes within FZ5 and FZ6 suggests a relationship between the BSR and the faults. The gas chimneys located here probably originate from and are rooted beneath the BSR (e.g., Auguy et al., 2017). Furthermore, the chimneys in the West–volume–(e), are elongated in the orientation of the (NNW–SSE) BSR–ridges (Figure 8f). |
| BSR depth | The BSR lies below H3 in the east of the volume, then increases in thickness (i.e., depth) towards the west. |

***Supplementary Tables***

| **TEW–volume** |
|---|
| Survey configuration |
| Ship's speed: 4kn ± 0.3 knots<br>Gun system: Two mini-GI (30/30 inch$^3$ and 15/15 inch$^3$)<br>Shooting pressure: ~170-180 bar<br>Shooting interval: 6 sec<br>Recording window: 3.5 sec<br>Recording delay: 0 sec<br>Sampling interval: 0.25 milliseconds (ms)<br>3D survey line number count: 31<br>Streamer depth: 1.5 m (streamer depth increased from line 25 after losing buoyancy on the cross-cable of the P-cable system). |
| Volume dimensions |
| In-line range: 2 - 328 - 1; Total: 327<br>Cross-line range: 445 - 1551 - 1; Total: 1107<br>Z range (m): 1191.000 - 1520.130 - 0.207; Total: 1591<br>Inl/Crl bin size: 6.25 / 6.25 (m/line)<br>Area: 14.15 (km$^2$)<br>In-line orientation: 125.06° clockwise from N |

***Table S–1****. High–resolution 3D seismic survey configurations and volume dimensions for the TEW–volume.*

| **West–volume** |
| --- |
| Survey configuration |
| Ship's speed: 4kn ± 0.3 knot<br>Gun system: Two mini-GI (30/30 inch$^3$ and 15/15 inch$^3$)<br>Shooting pressure: ~170-180 bar<br>Shooting interval: 6 sec<br>Recording window: 3.5 sec<br>Recording delay: 0 sec<br>Sampling interval: 0.25 milliseconds (ms)<br>Survey line number count: 23<br>Streamer depth: 1.5 m |
| Volume dimensions |
| In-line range: 8 - 225 - 1; Total: 218<br>Cross-line range: 223 - 1681 - 1; Total: 1459<br>Z range (m): 1370.000 – 1811.258 - 0.293; Total: 1507<br>Inl/Crl bin size: 6.25 / 6.25 (m/line)<br>Area: 12.42 (km$^2$)<br>In-line orientation: 121.80° clockwise from N |

***Table S–2****. High–resolution 3D seismic survey configurations and volume dimensions for the West–volume.*

| H0.3 (~0.1 Ma) | H1 (~0.2 Ma) | H2 (~0.4 Ma) | H2.25 (~1 Ma) |
|---|---|---|---|
| 8a | 8a | 41c | 64a |
| | 44 | 64c | 56 |
| | 9a | 12b | 4a |
| | 1 | 57 | 3a |
| | 29a | 56 | 10 |
| | | 8a | 52a |
| | | 4a | 1 |
| | | 3a | 5a |
| | | 10 | 61f |
| | | 9a | 29c |
| | | 52a | 26c |
| | | 1 | 50b |
| | | 5a | 6a |
| | | 48 | |
| | | 63a | |

***Table S–3***. *Fault plane age burial zones (arbitrarily defined) for the TEW–volume (groups: Y–1 = yellow, G–2 = green, B–3 = blue, O–4 = orange, P–5 = pink).*

| H0.3 (~0.1 Ma) | H1 (~0.2 Ma) | H2 (~0.4 Ma) | H2.25 (~1 Ma) | H3 (~1.5 Ma) |
|---|---|---|---|---|
| 15 | 15 | 34c | 34c | 44 |
| 61 | 11b | 34e | 32b | 34c |
| 9c | 85 | 29c | 29c | 34d |
| 9b | 9b | 15 | 14c | 32b |
| 5 | 5 | 11a | 49a | 29b |
| | 118 | 9b | 9a | 14c |
| | | 5 | | 14g |
| | | 50b | | 8f |
| | | | | 8b |
| | | | | 8d |
| | | | | 10g |
| | | | | 10f |

***Table S–4***. *Fault plane age burial zones (arbitrarily defined) for the West–volume (groups: Y–1 = yellow, G–2 = green, B–3 = blue, O–4 = orange, P–5 = pink).*

| Horizon | Fault plane | Age zone† | Size (S/ M/ L) | Dip direction | Throw (m) (mostly at limit of resolution <3m) | Feature associated with structure |
|---|---|---|---|---|---|---|
| H0.3 | 8a | P–5 | M | SW | < 3 | |
| H1 | 8a | P–5 | M | SW | < 3 | |
| | 44 | O–4 | S | ? | no (distorted) | CHY* (pull |
| | 9a | O–4 | S | NW | < 3 | up) / edge* |
| | 1 | Y–1 | L | SW | < 3 (?)* | |
| | 29a | O–4 | S | SW | < 3 | |
| H2 | 41c | B–3 | S | - | no | PM* (above) |
| | 64c | B–3 | S | - | no | |
| | 12b | B–3 | S | - | no | PM (above) |
| | 57 | B–3 | S | - | no | CHY |
| | 56 | G–2 | S | - | no | |
| | 8a | P–5 | L | SW | < 3 | |
| | 4a | Y–1 | L | SW | < 3 | CHY / PM |
| | 3a | G–2 | M | - | no | (above) |
| | 10 | G–2 | M | SW | 15 | |
| | 9a | O–4 | M | NW | < 3 | CHY / FZ* |
| | 52a | O–4 | L | NW | < 3 | |
| | 1 | Y–1 | L | ? | < 3 (?) | |
| | 5a | Y–1 | L | SW | < 3 (?) | |
| | 48 | O–4 | M | NE | < 3 | |
| | 63a | O–4 | S | SW | < 3 | CHY (pull up) |
| H2.25 | 64a | G–2 | M | - | no | |
| | 56 | G–2 | S | - | no | |
| | 4a | Y–1 | L | SW | < 3 | |
| | 3a | G–2 | M | - | no | |
| | 10 | G–2 | M | SW | 15 | CHY / FZ |
| | 52a | O–4 | L | NW | < 3 | |
| | 1 | Y–1 | L | SW | < 3 (?) | |
| | 5a | Y–1 | L | ? | < 3 (?) | |
| | 61f | B–3 | S | SE | < 3 | |
| | 29c | B–3 | S | NE | < 3 | |
| | 26c | B–3 | S | NW | < 3 | |
| | 50b | B–3 | M | ? | < 3 (?) | |
| | 6a | B–3 | M | NW | < 3 (?) | |

***Table S–5****. Characteristics of fault planes with throw values in the TEW–volume (*PM = pockmark, CHY = chimney, edge = edge of survey, (?) = at resolution limit, FZ = within fault zone, "no" = no throw measured, †refer to* ***Table S–3****).*

| Horizon | Fault plane | Age zone† | Size (S/M /L) | Dip direction | Throw (m) (mostly at limit of resolution <4 m) | Feature associated with structure |
|---|---|---|---|---|---|---|
| H0.3 | 15 | P–5 | S | SW | < 4 | |
| | 61 | P–5 | S | NE | < 4 | |
| | 9c | P–5 | S | SW | < 4 | PM* |
| | 9b | O–4 | S | SW | no (distorted) | PM |
| | 5 | P–5 | M | SW | < 4 | PM |
| H1 | 15 | P–5 | S | SW | < 4 | |
| | 11b | P–5 | S | NE | < 4 | CHY* |
| | 85 | O–4 | S | S | < 4 | |
| | 9b | O–4 | M | SW | no (distorted) | PM |
| | 5 | P–5 | M | SW | < 4 | PM |
| | 118 | O–4 | S | SW | < 4 | |
| H2 | 34c | B–3 | L | SW | < 4 | |
| | 34e | B–3 | S | SW | < 4 | |
| | 29c | B–3 | M | S | < 4 | |
| | 15 | P–5 | S | SW | < 4 | |
| | 11a | B–3 | S | NE | < 4 | |
| | 9b | O–4 | M | SW | no (distorted) | PM |
| | 5 | P–5 | M | SW | < 4 | |
| | 50b | B–3 | S | SW | no (distorted) | PM |
| H2.25 | 34c | B–3 | L | SW | < 4 | |
| | 32b | G–2 | L | S | < 4 | |
| | 29c | B–3 | M | S | < 4 | |
| | 14c | G–2 | L | S/SE | 7 | |
| | 49a | G–2 | S | SW | < 4 | AA* – PM |
| | 9a | G–2 | M | SW | < 4 | PM (above) |
| H3 | 44 | Y–1 | S | SE | < 4 | |
| | 34c | B–3 | L | SW | < 4 | |
| | 34d | Y–1 | S | S | < 4 | CHY |
| | 32b | G–2 | L | S | < 4 | |
| | 29b | Y–1 | S | S | 6 | |
| | 14c | G–2 | L | S | 7 | |
| | 14g | Y–1 | S | SE | 6 | |
| | 8f | Y–1 | S | SW | 7 | PM (above) |
| | 8b | Y–1 | S | SW | 10 | PM (above) |
| | 8d | Y–1 | S | SW | 6 | PM (above) |
| | 10g | Y–1 | S | SW | < 4 | |
| | 10f | Y–1 | S | SW | no (distorted) | PM (above) |

***Table S–6**. Characteristics of fault planes with throw values in the West–volume (* PM = pockmark, CHY = chimney, AA = amplitude anomaly, "no" = no throw measured, †refer to **Table S–4**).*

| Horizon | Fault plane | Age zone† | Azimuth (A) | Dip (Z) |
|---|---|---|---|---|
| H0.3 | 8a | P–5 | 24 | 63 |
| H1 | 8a | P–5 | 24 | 63 |
| | 44 | O–4 | 4 | 63 |
| | 9a | O–4 | 67 | 62 |
| | 1 | Y–1 | 157 | 58 |
| | 29a | O–4 | 154 | 52 |
| H2 | 41c | B–3 | 167 | 54 |
| | 64c | B–3 | 124 | 63 |
| | 12b | B–3 | 156 | 54 |
| | 57 | B–3 | 92 | 46 |
| | 56 | G–2 | 131 | 50 |
| | 8a | P–5 | 24 | 63 |
| | 4a | Y–1 | 7 | 57 |
| | 3a | G–2 | 35 | 56 |
| | 10 | G–2 | 161 | 49 |
| | 9a | O–4 | 67 | 62 |
| | 52a | O–4 | 78 | 57 |
| | 1 | Y–1 | 157 | 58 |
| | 5a | Y–1 | 153 | 59 |
| | 48 | O–4 | 129 | 61 |
| | 63a | O–4 | 136 | 59 |
| H2.25 | 64a | G–2 | 112 | 43 |
| | 56 | G–2 | 131 | 50 |
| | 4a | Y–1 | 7 | 57 |
| | 3a | G–2 | 35 | 56 |
| | 10 | G–2 | 161 | 49 |
| | 52a | O–4 | 78 | 57 |
| | 1 | Y–1 | 157 | 58 |
| | 5a | Y–1 | 153 | 59 |
| | 61f | B–3 | 86 | 58 |
| | 29c | B–3 | 154 | 60 |
| | 26c | B–3 | 51 | 53 |
| | 50b | B–3 | 92 | 61 |
| | 6a | B–3 | 38 | 53 |

***Table S–7****. Fault plane dip (° from horizontal) and azimuth (° clockwise from north) and assigned age zone (†refer to* ***Table S–3****) in the TEW–volume.*

| Horizon | Fault plane | Age zone† | Azimuth (A) | Dip (Z) |
|---|---|---|---|---|
| H0.3 | 15 | P–5 | 114 | 52 |
| | 61 | P–5 | 129 | 48 |
| | 9c | P–5 | 161 | 46 |
| | 9b | O–4 | 155 | 47 |
| | 5 | P–5 | 157 | 55 |
| H1 | 15 | P–5 | 114 | 52 |
| | 11b | P–5 | 130 | 56 |
| | 85 | O–4 | 93 | 60 |
| | 9b | O–4 | 155 | 47 |
| | 5 | P–5 | 157 | 55 |
| | 118 | O–4 | 104 | 61 |
| H2 | 34c | B–3 | 139 | 58 |
| | 34e | B–3 | 128 | 41 |
| | 29c | B–3 | 114 | 48 |
| | 15 | P–5 | 114 | 52 |
| | 11a | B–3 | 130 | 56 |
| | 9b | O–4 | 155 | 47 |
| | 5 | P–5 | 157 | 55 |
| | 50b | B–3 | 174 | 63 |
| H2.25 | 34c | B–3 | 139 | 58 |
| | 32b | G–2 | 97 | 56 |
| | 29c | B–3 | 114 | 48 |
| | 14c | G–2 | 96 | 55 |
| | 49a | G–2 | 152 | 64 |
| | 9a | G–2 | 152 | 62 |
| H3 | 44 | Y–1 | 113 | 59 |
| | 34c | B–3 | 139 | 58 |
| | 34d | Y–1 | 146 | 45 |
| | 32b | G–2 | 97 | 56 |
| | 29b | Y–1 | 110 | 49 |
| | 14c | G–2 | 96 | 55 |
| | 14g | Y–1 | 85 | 62 |
| | 8f | Y–1 | 149 | 52 |
| | 8b | Y–1 | 157 | 55 |
| | 8d | Y–1 | 152 | 48 |
| | 10g | Y–1 | 153 | 62 |
| | 10f | Y–1 | 169 | 44 |

***Table S–8****. Fault plane dip (° from horizontal) and azimuth (° clockwise from north) and assigned age zone (†refer to* ***Table S–4****) in the West–volume.*

| Chimney ID | Pockmark ID | Width (m) | Length (m) | Ratio (W: L) | Surface area ($m^2$) | Orientation (deg) |
|---|---|---|---|---|---|---|
| **C–W1** | 1 | 170 | 216 | 0.79 | 26201 | 157 |
| **C–W2** | 5 | 168 | 189 | 0.89 | 25039 | 177 |
| **C–W3** | 3 | 135 | 209 | 0.65 | 18650 | 165 |
| **C–E1** | 15 | 201 | 210 | 0.96 | 33895 | 0 |
| **C–E2** | 13 | 107 | 144 | 0.74 | 10454 | 115 |
| **C–E4** | 14 | 208 | 285 | 0.73 | 47430 | 134 |

***Table S–9****. Pockmark characteristics for horizon SF in the TEW–volume–*(*e) and TEW–volume–*(*w).*

| Chimney ID | Pockmark ID | Width (m) | Length (m) | Ratio (W: L) | Surface area ($m^2$) | Orientation (deg) |
|---|---|---|---|---|---|---|
| **C–W3** | 1 | 60 | 85 | 0.70 | 3228 | 42 |
| **C–E1** | 16 | 204 | 231 | 0.88 | 38966 | 157 |
| **C–E2** | 13 | 181 | 260 | 0.70 | 35841 | 178 |
| **C–E3** | 11 | 156 | 217 | 0.72 | 24326 | 10 |
| **C–E4** | 14 | 220 | 426 | 0.52 | 76836 | 29 |

***Table S–10****. (Paleo) Pockmark characteristics for horizon H1 in the TEW–volume–*(e) *and TEW–volume–*(*w).*

| Chimney ID | Pockmark ID | Width (m) | Length (m) | Ratio (W: L) | Surface area ($m^2$) | Orientation (deg) |
|---|---|---|---|---|---|---|
| **C–7** | 1 | 91 | 125 | 0.72 | 7437 | 136 |
| – | 2 | 149 | 232 | 0.64 | 21567 | 12 |
| – | 3 | 159 | 494 | 0.32 | 43971 | 164 |
| – | 4 | 289 | 616 | 0.47 | 104232 | 159 |
| – | 5 | 149 | 170 | 0.87 | 18934 | 0 |
| – | 6 | 193 | 506 | 0.38 | 55573 | 173 |

***Table S–11****. Pockmark characteristics for horizon SF in the West–volume–(e) and West–volume–(w).*

| Chimney ID | Pockmark ID | Width (m) | Length (m) | Ratio (W: L) | Surface area ($m^2$) | Orientation (deg) |
|---|---|---|---|---|---|---|
| **C–1** | 1 | 68 | 144 | 0.47 | 4243 | 21 |
| – | 4 | 141 | 171 | 0.82 | 17666 | 135 |
| – | 5 | 147 | 228 | 0.64 | 22203 | 157 |
| – | 3 | 120 | 167 | 0.72 | 13496 | 147 |
| – | 2 | 184 | 276 | 0.67 | 35163 | 175 |

***Table S–12****. (Paleo) Pockmark characteristics for horizon H1 in the West–volume–(e) and West–volume–(w).*

| Chimney ID | Pockmark ID | Width (m) | Length (m) | Ratio (W: L) | Surface area ($m^2$) | Orientation (deg) |
|---|---|---|---|---|---|---|
| – | 1 | 147 | 210 | 0.70 | 19977 | 0 |
| **C–5** | 4 | 303 | 431 | 0.70 | 95858 | 80 |
| – | 2 | 196 | 252 | 0.78 | 35516 | 47 |
| **C–3** | 5 | 209 | 333 | 0.63 | 44157 | 45 |
| **C–4** | 6 | 167 | 345 | 0.48 | 37006 | 135 |

***Table S–13****. (Paleo) Pockmark characteristics for horizon H3 in the West–volume–(w).*

***Supplementary Figures***

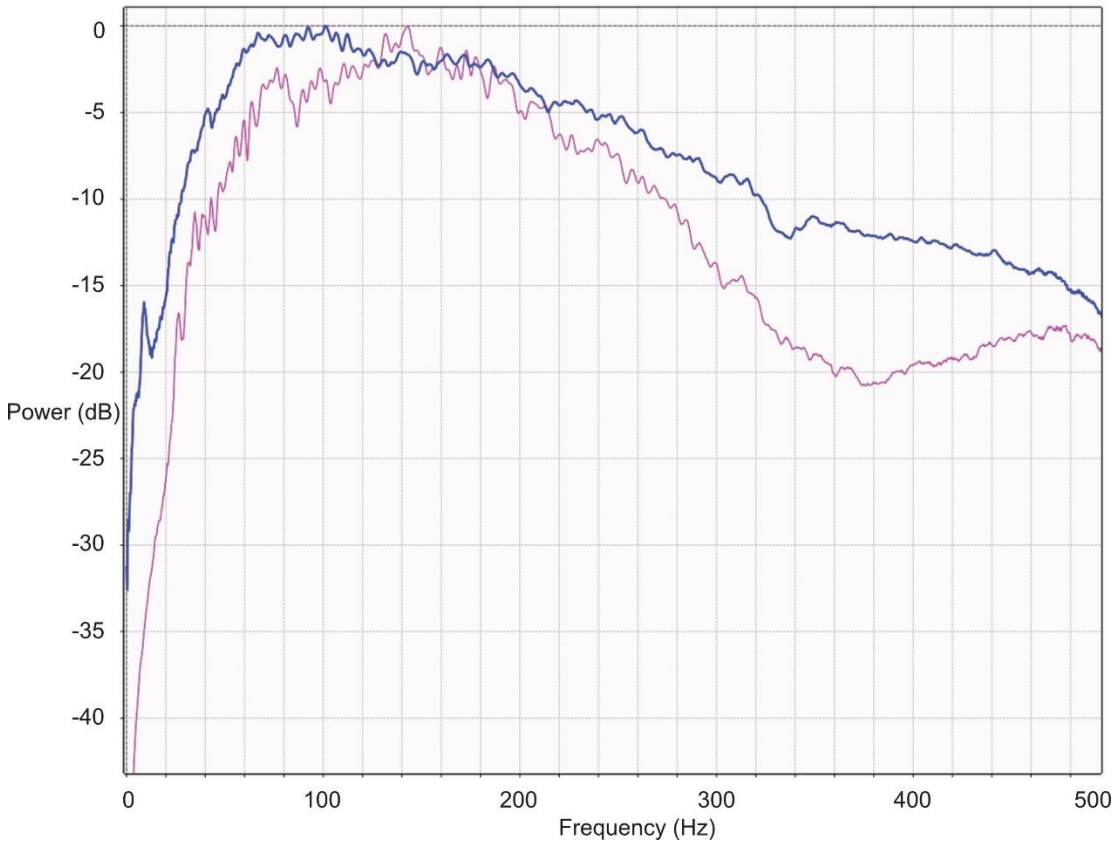


***Figure S–1.*** *Amplitude spectra for the TEW–volume (purple line) and the West–volume (blue line). The dominant frequencies are ~120 Hz and ~100 Hz respectively.*

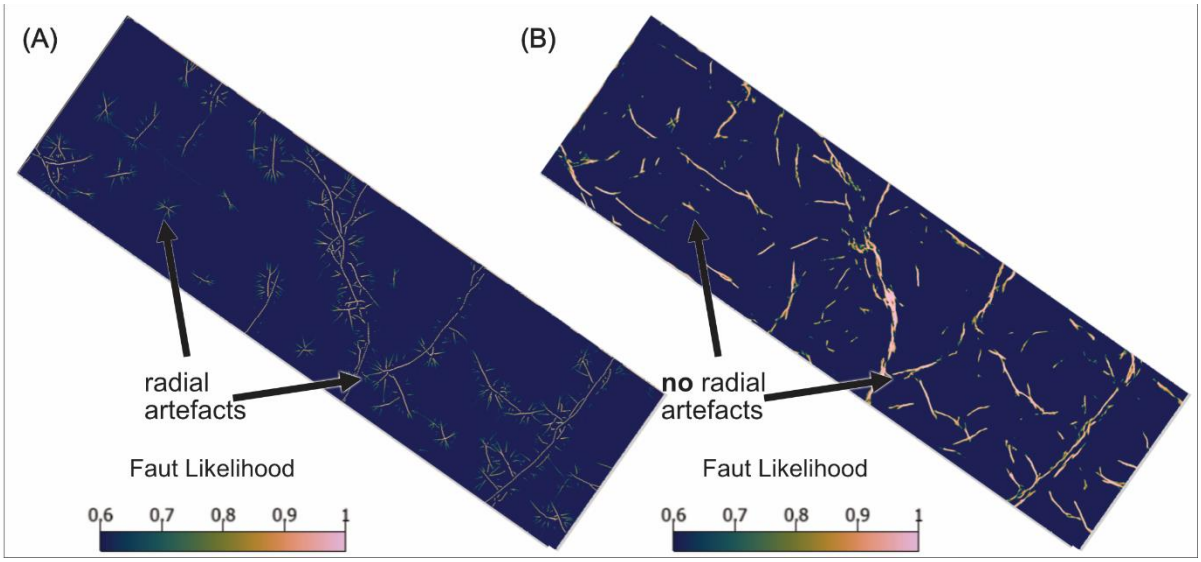


***Figure S–2****. Comparing the two different fault likelihood volumes using TEW–volume/horizon H2 as an example.* ***(A)*** *"original" fault likelihood with computational time of 52 minutes.* ***(B)*** *ML fault likelihood volume (used in the study) with computational time of six minutes.*

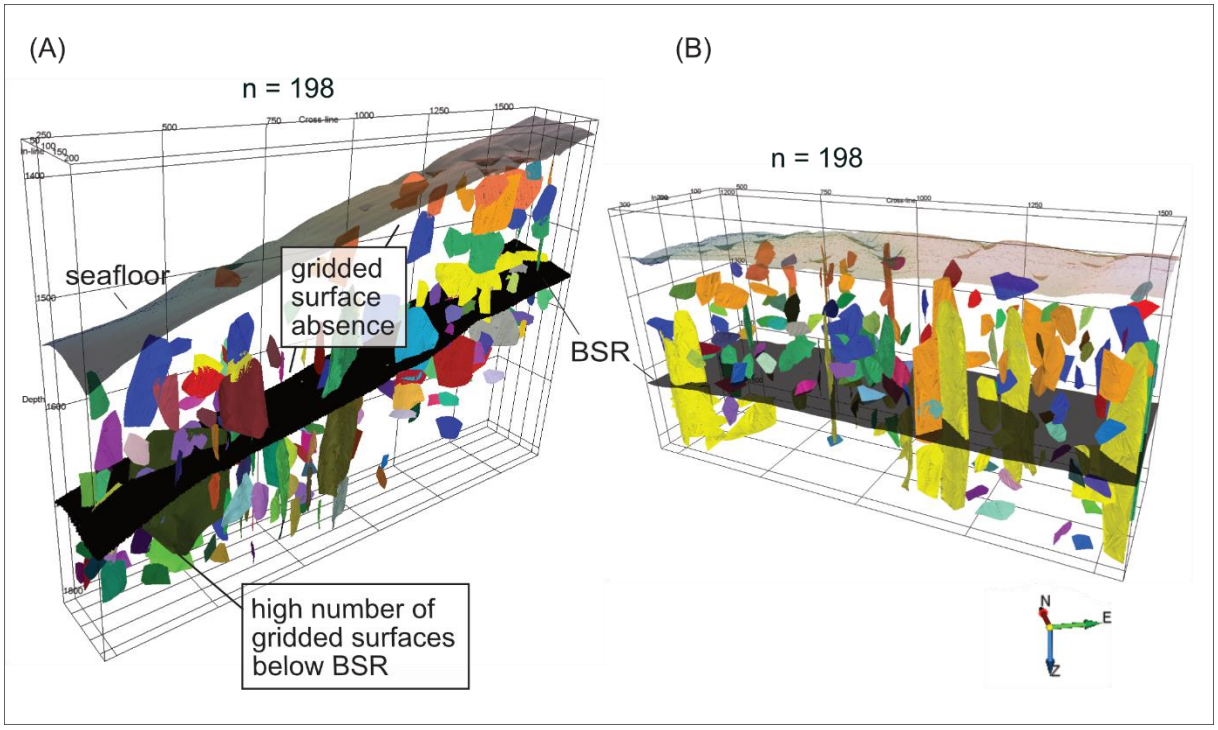


***Figure S–3***. *Gridded surface volume displaying all 198 fault planes for each high-resolution 3D volume, viewed together with the BSR (semi–transparent black surface), and seafloor (semi–transparent colored horizon).* ***(A)*** *Fault planes are less evenly distributed in the West–volume. A high density of gridded surfaces occurs below the BSR surface in the west of the West–volume as the seafloor deepens, and the thickness of sediments reduces towards the flank of the Ridge. There are fewer extractions above the BSR surface than below in the center of the volume (i.e., labeled "gridded surface absence").* ***(B)*** *The fault planes are more evenly distributed in the TEW–volume and there are proportionately more gridded surfaces above the BSR.*

*Rose diagram, Stereonet Pole Plots and Kamb contours*

The stereonets (which are lower hemisphere projections) were created using R. W. Allmendinger (2020) software "Stereonet v. 11". The planar features are displayed as poles to planes. The Kamb (1959) method was used for contouring. This method uses a variable area counting circle depending on the number of data points. The rose plot is the analysis of the input planes (AZ) with petals parallel to the strike direction. The petals are scaled by area with 10° bin size.

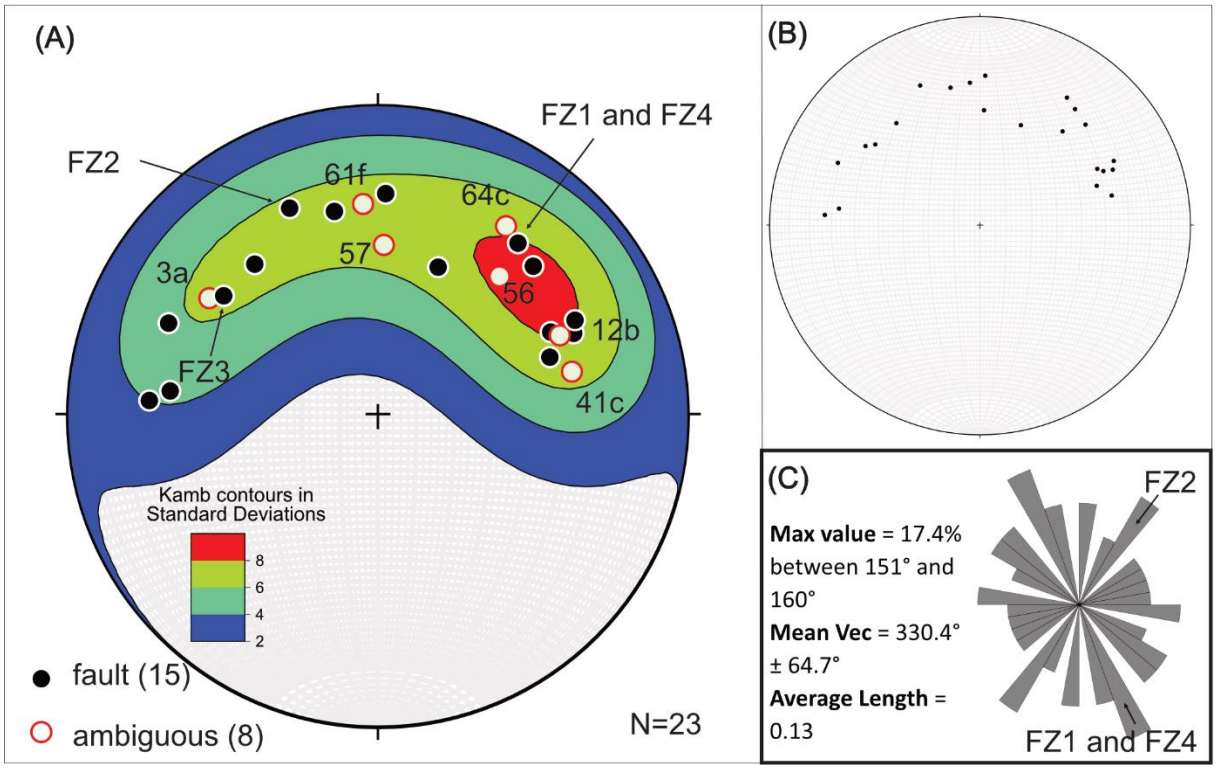


***Figure S–4**. **(A)** TEW–volume contoured pole plot. The poles are defined by those that are faults (black circles) and those that are ambiguous features (open red circles and annotated). The purpose of the contoured plot is to show where the fault planes are clustered. The ambiguous poles are within the range of the fault planes indicating that the structures are probably related. **(B)** Non-contoured pole plot for all fault planes. **(C)** Rose plot showing the maximum petal value between 151° and 160°, which aligns with the fault zones (FZ) FZ1 and FZ4. The contoured pole and rose plots are annotated with fault zones. The largest petals (scaled by area) are in the orientation of FZ1/FZ4 (NNW-SSE) and FZ2 (NE-SW).*

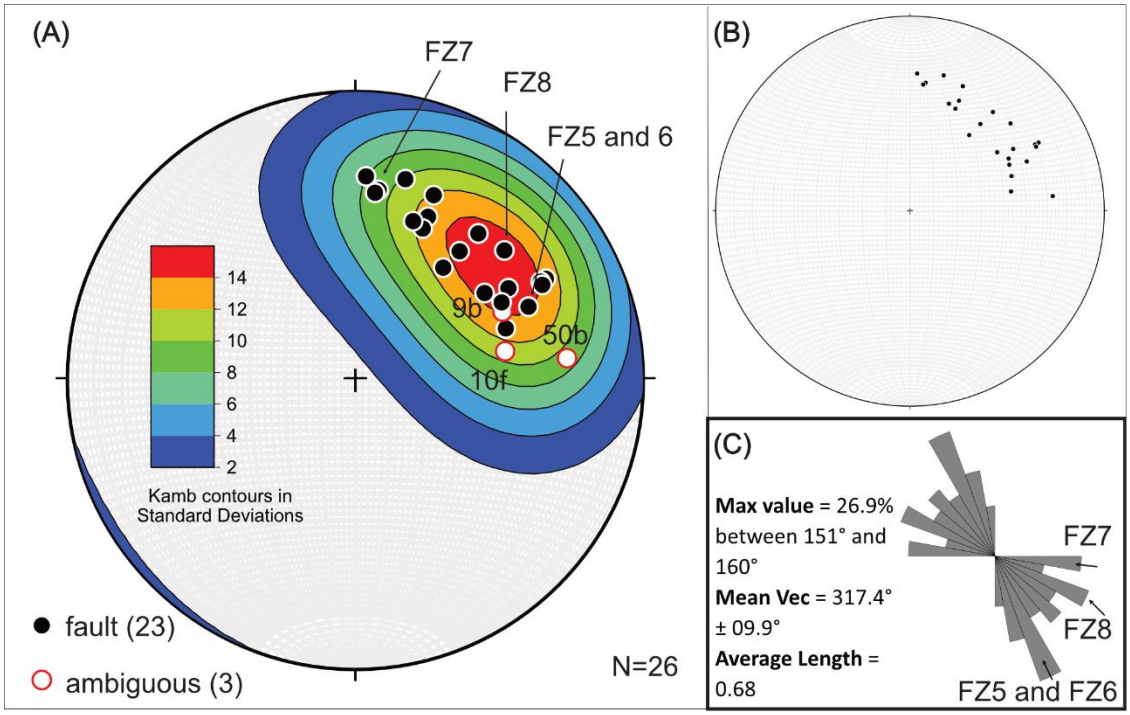


***Figure S–5***. ***(A)*** *West–volume contoured pole plot. The poles are defined by those that are faults (black circles) and those that are ambiguous features (open red circles and annotated). The purpose of the pole plot is to show where the fault planes are clustered. There are fewer ambiguous features in the West–volume as compared with the TEW–volume and they lie within the contours. The orientations of fault zones (FZ) FZ5, FZ6 and FZ8 lie within the highest clustering of poles in NNW-SSE and NW-SE orientation.* ***(B)*** *Non-contoured pole plot for all fault planes.* ***(C)*** *Rose plot showing the largest petals (scaled by area) between 151° and 160°, which is consistent with the results from the TEW–volume. The orientation NNW-SSE (FZ5 and FZ6) is dominant among all fault planes.*

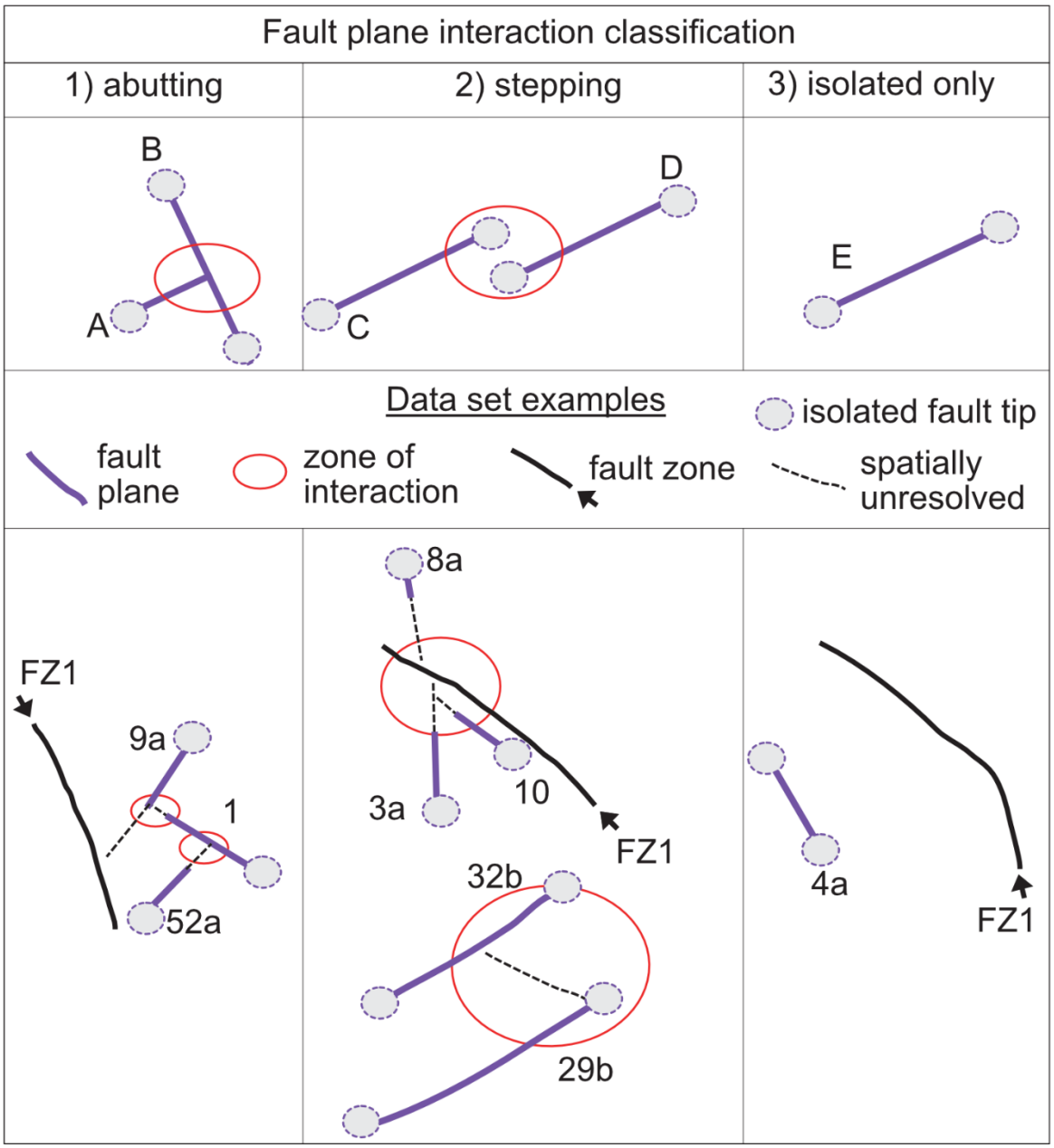


***Figure S–6**. Fault plane interaction classification (after Peacock et al., 2017) with examples from the study.*

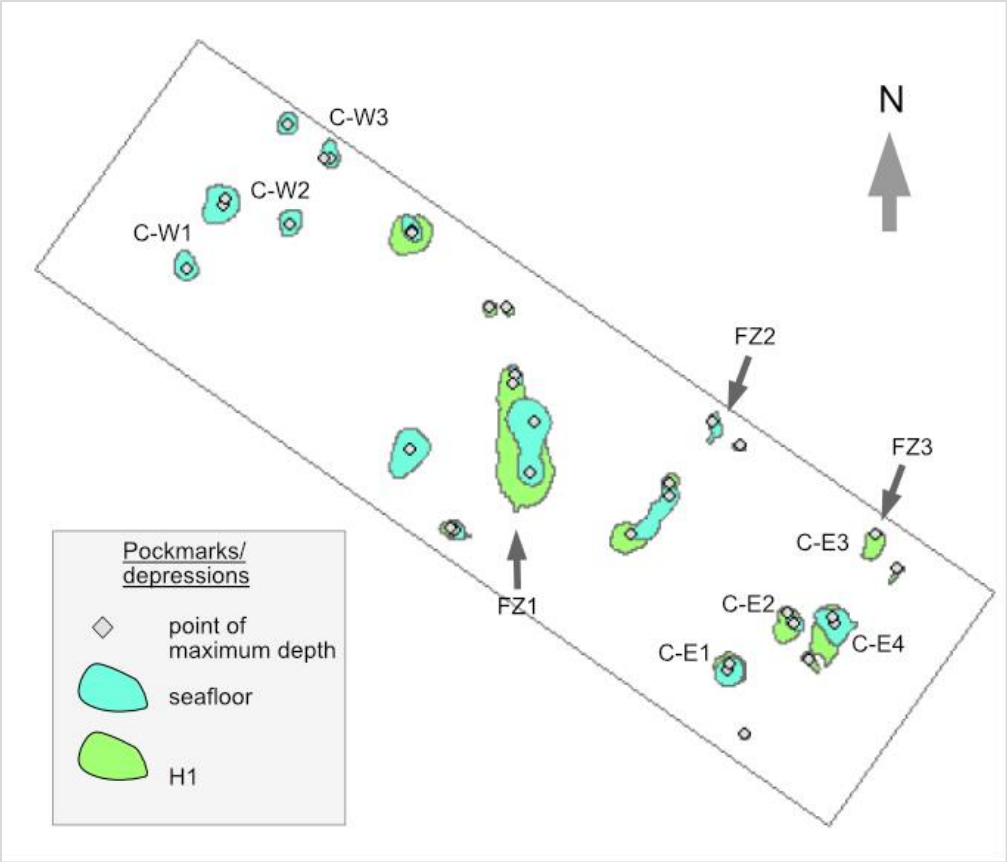


***Figure S–7****. TEW–volume survey area showing extracted pockmarks/depressions from 2 surfaces: seafloor (SF) and H1 (10 x 10 m). Refer to* ***Supplementary Table S–9*** *for pockmark characteristics for the SF surface in the TEW–volume–(w) (****C–W1****,* ***C–W2*** *and* ***C–W3****) and TEW–volume–(e) (****C–E1****,* ***C–E2*** *and* ***C–E4****); and* ***Supplementary Table S–10*** *for paleo pockmark characteristics for surface H1 in the TEW–volume–(w) (****C–W3****) and TEW–volume–(e) (****C–E1****,* ***C–E2****,* ***C–E3*** *and* ***C–E4****). Note: There are no pockmark extractions at H1 for chimneys* ***C–W1*** *and* ***C–W2****, and there is no pockmark extraction for* ***C–E3*** *at the SF. Gray filled diamonds represent the maximum depth for all the pockmark extractions for surfaces SF and H1.*

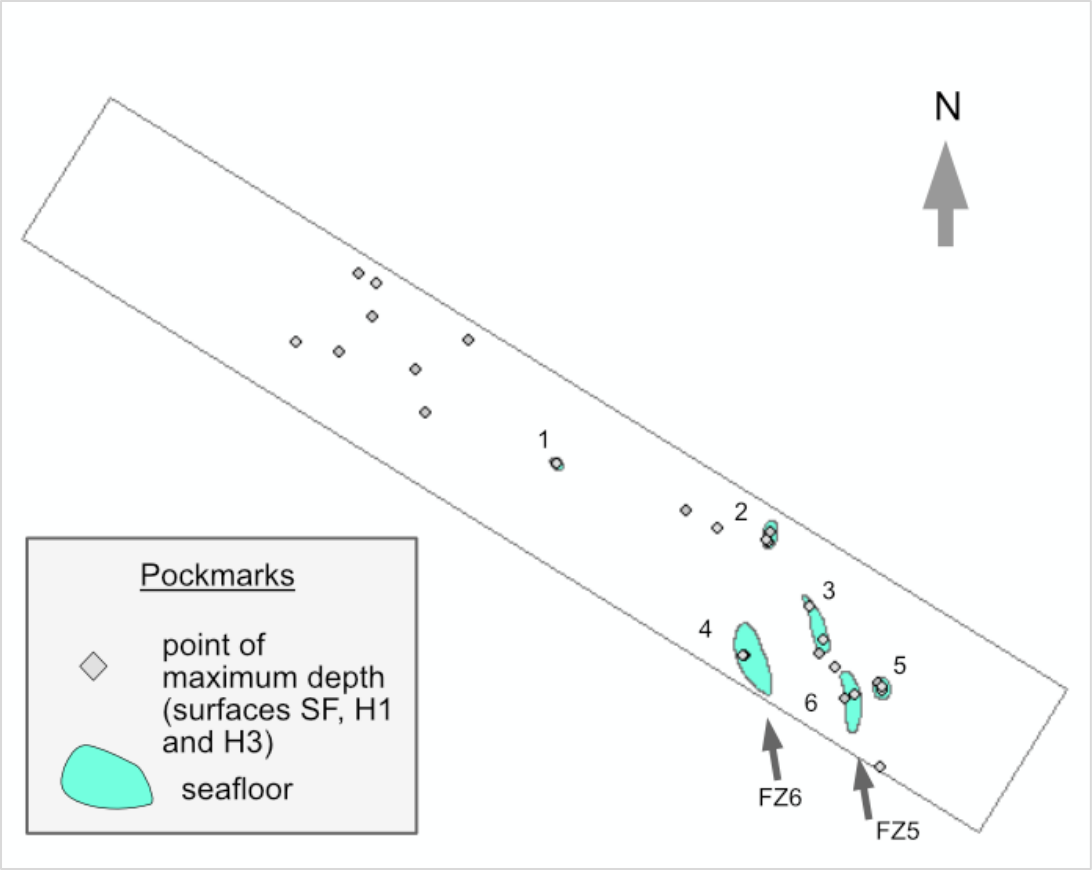


***Figure S–8***. *West–volume survey area showing extracted pockmarks/depressions from the seafloor surface (SF) (10 x 10 m). Refer to* ***Supplementary Table S–11*** *for pockmark characteristics in the West–volume–(w) area (**1**) (i.e., **C–7**) and West–volume–(e) area (**2–6**). Gray filled diamonds represent maximum depth for all the pockmark extractions for surfaces SF, H1 and H3.*

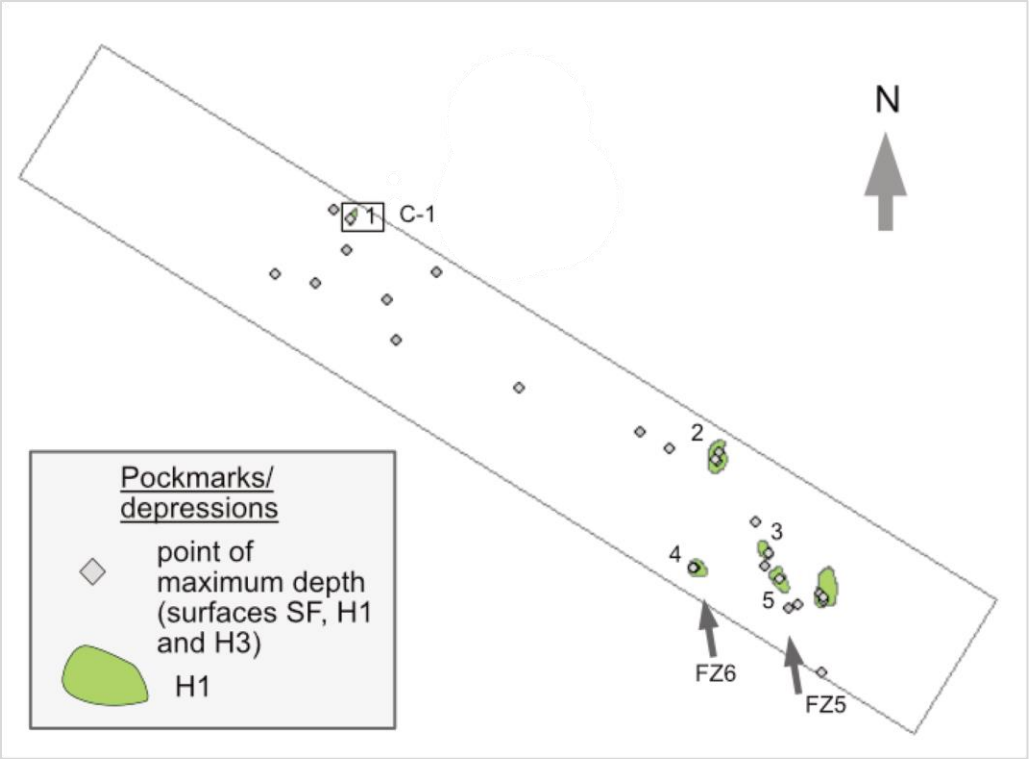


***Figure S–9***. *West–volume survey area showing extracted paleo pockmarks/depressions from surface H1 (10 x 10 m). Refer to* ***Supplementary Table S–12*** *for paleo pockmark characteristics in the West–volume–(w) area (**1**) (i.e., **C–1**) and West–volume–(e) area (**2-5**). Gray filled diamonds represent maximum depth for all the pockmark extractions for the seafloor, H1 and H3 surfaces.*

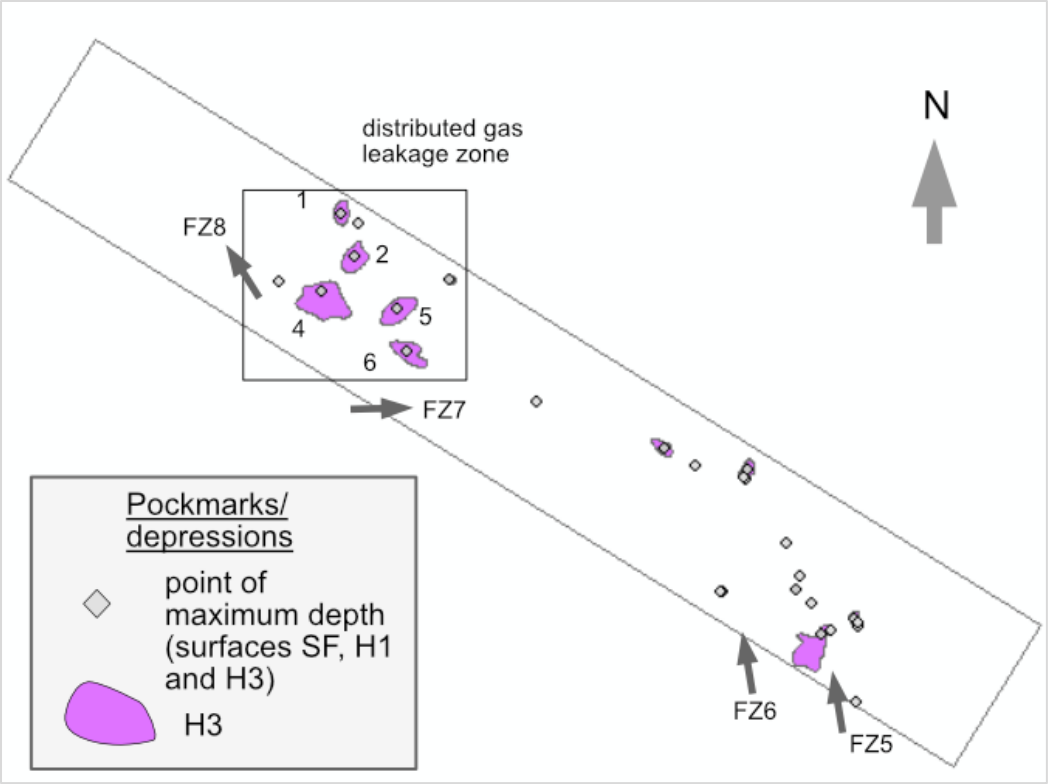


***Figure S–10****. West–volume survey area showing extracted paleo pockmarks/depressions from H3 surface (10 x 10 m). Refer to* ***Supplementary Table S–13*** *for pockmark characteristics in the West–volume–(w) area (****1, 2, 4- 6****) within the distributed gas leakage zone between fault zones FZ7 and FZ8. Gray filled diamonds represent the maximum depth for all the pockmark extractions for the seafloor, H1 and H3 surfaces.*

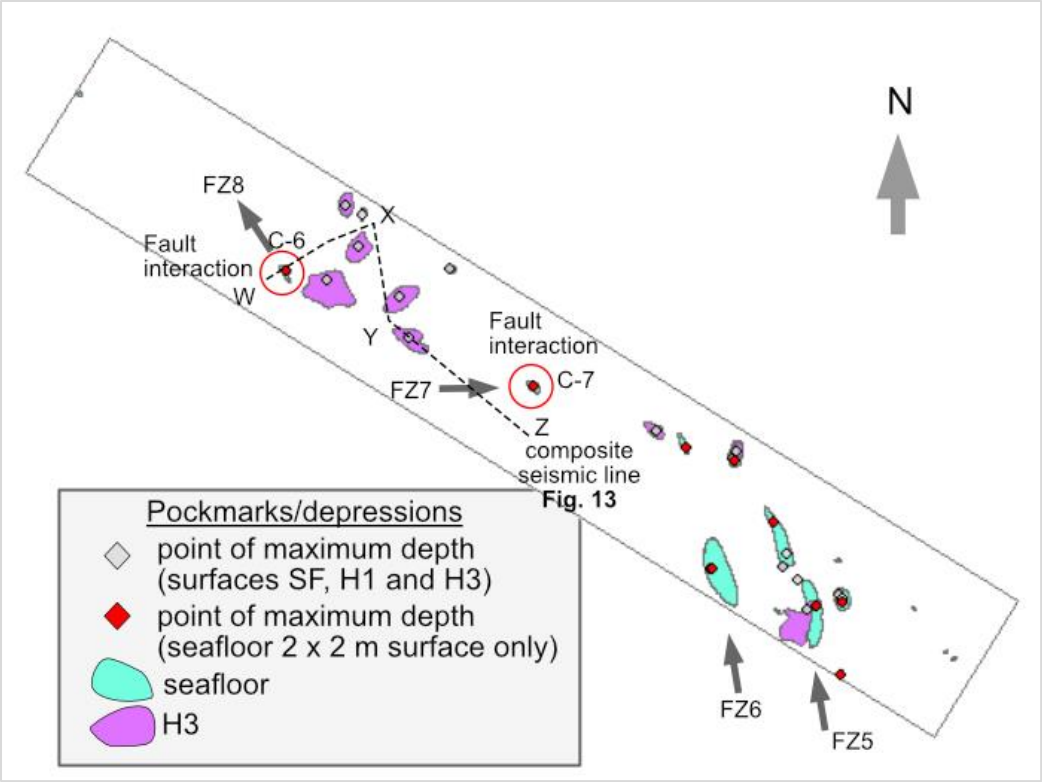


***Figure S–11.*** *West–volume survey area showing extracted pockmarks/depressions from 2 (10 x 10 m) surfaces: seafloor (SF) and H3. A 2 x 2 m surface was created to test the minimum pockmark extraction revealing smaller seafloor pockmarks (encircled in red). In fault zone FZ8 the red circle shows a small pockmark intersecting the composite seismic line (dashed black line). Gray filled diamonds represent the maximum depth for the pockmark extractions for the SF and H3 surfaces, and the red filled diamonds represent the maximum depth for the 2 x 2 m surface seafloor pockmarks. Pockmark widths for the 2 x 2 m surfaces are between 65 and 90 m.* ***Figure 8f*** *displays faults interacting beneath the pockmark (encircled in red) at the center of the survey (**C–7**).* ***Figure 13*** *displays the emergent chimneys and seafloor pockmarks (**C–6** and **C–1**, i.e., at points **"W" and "X"** respectively) elongated in the same orientation as the fault zones FZ5 and FZ6.*